ACS OMEGA

Open Access

http://pubs.acs.org/journal/acsodf

Article

Combined *In Silico* and *In Vitro* Study to Reveal the Structural Insights and Nucleotide-Binding Ability of the Transcriptional Regulator PehR from the Phytopathogen *Ralstonia solanacearum*

Mohit Yadav,[#] Sharmilee Sarkar,[#] Kaushika Olymon, Suvendra Kumar Ray,[*] and Aditya Kumar[*]

Cite This: *ACS Omega* 2023, 8, 34499−34515

Read Online

ACCESS | Metrics & More | Article Recommendations | Supporting Information

ABSTRACT: The transcriptional regulator PehR regulates the synthesis of the extracellular plant cell wall-degrading enzyme polygalacturonase, which is essential in the bacterial wilt of plants caused by one of the most devastating plant phytopathogens, *Ralstonia solanacearum*. The bacterium has a wide global distribution infecting many different plant species, resulting in massive agricultural and economic losses. Because the PehR molecular structure has not yet been determined and the structural consequences of PehR on ligand binding have not been thoroughly investigated, we have used an *in silico* approach combined with *in vitro* experiments for the first time to characterize the PehR regulator from a local isolate (Tezpur, Assam, India) of the phytopathogenic bacterium *R. solanacearum* F1C1. In this study, an *in silico* approach was employed to model the 3D structure of the PehR regulator, followed by the binding analysis of different ligands against this regulatory protein. Molecular docking studies suggest that ATP has the highest binding affinity for the PehR regulator. By using molecular dynamics (MD) simulation analysis, involving root-mean-square deviation, root-mean-square fluctuations, hydrogen bonding, radius of gyration, solvent-accessible surface area, and principal component analysis, it was possible to confirm the sudden conformational changes of the PehR regulator caused by the presence of ATP. We used an *in vitro* approach to further validate the formation of the PehR-ATP complex. In this approach, recombinant DNA technology was used to clone, express, and purify the gene encoding the PehR regulator from *R. solanacearum* F1C1. Purified PehR was used in ATP-binding experiments using fluorescence spectroscopy and Fourier transform infrared spectroscopy, the outcomes of which showed a potent binding to ATP. The putative PehR-ATP-binding analysis revealed the importance of the amino acids Lys[190], Glu[191], Arg[192], Arg[375], and Asp[378] for the ATP-binding process, but further study is required to confirm this. It will be simpler to comprehend the catalytic mechanisms of a crucial PehR regulator process in *R. solanacearum* with the aid of the ATP-binding process hints provided by these structural biology applications.

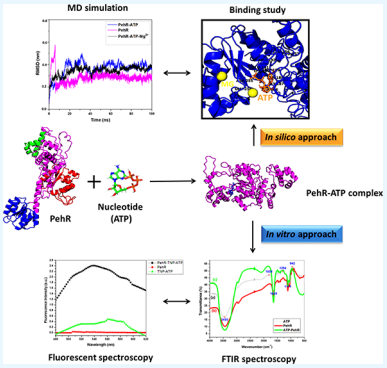

INTRODUCTION

The devastating soil-borne disease known as bacterial wilt is prevalent worldwide and affects hundreds of plant species, particularly several important crops in the *Cucurbitaceae* and *Solanaceae* families.[1] Bacterial wilt is a factor in the deterioration of soil, poor plant development, excess of harmful bacteria, and disease outbreaks that are spread through the soil.[2] This has led to the theory that wilting results from an altered ecological balance between plants and rhizosphere microorganisms.[3] Due to the wide geographical distribution of *Ralstonia solanacearum*, the existence of numerous variants, its persistence, and the wide variety of hosts it affects, bacterial wilt control has been a problem on a global scale without any practical solutions having been developed.

Bacterial wilt is a global disease caused by the Gram-negative bacterium *R. solanacearum*.[4] More than 450 species of plants in over 50 families are susceptible to the extremely harmful soil-borne pathogen *R. solanacearum*.[5,6] The host plants for *R. solanacearum* include a variety of significant commercial crops, such as tomatoes, tobacco, potatoes, and peanut. *R. solanacearum* can cause a wide range of direct crop losses depending on the host, strain, cultivar, land type, and cropping technique. As an illustration, yield losses for tomatoes range from 0 to 91%, potatoes from 33 to 90%, tobacco from 10 to 30%, bananas from 80 to 100%, and groundnuts up to 20%.[4,7]

The life cycle of *R. solanacearum* is intricate, and the pathogen can endure for a very long time in soil and water.[8] When *R. solanacearum* strains detect root exudates, they use chemotaxis and flagellar movement to move to the host roots.[9,10] They move from the vascular bundle to the xylem after entering the root through injury, root tips, and other emerging sites. Once the bacterium enters the vascular system,

Received: May 8, 2023
Accepted: September 5, 2023
Published: September 16, 2023

Table 1. Comparative Features for PehR Structural Models

s. no.	feature	program	AlphaFold	I-TASSER	RaptorX	hybrid
1.	Ramachandran plot summary (residues in the most favored regions)	Procheck	91.6%	89.1%	86.5%	87.2%
		MolProbity	95.6%	91.8%	93.1%	92.4%
2.	raw score	Verify3D	0.16	0.18	0.22	0.22
		ProsaII	0.80	0.37	0.75	0.70
		Procheck	0.04	−1.02	−0.05	−0.13
		MolProbity	3.10	70.32	24.84	0.00
3.	Z-score	Verify3D	−4.82	−4.49	−3.85	−3.85
		ProsaII	0.62	−1.16	0.41	0.21
		Procheck	0.24	−6.03	−0.30	−0.77
		MolProbity	0.99	−10.54	−2.74	1.53
4.	RMS deviation (for bond angles)	PDB validation software	1.9°	3.7°	6.8°	2.7°
5.	RMS deviation (for bond lengths)	PDB validation software	0.012 Å	0.018 Å	0.096 Å	0.021 Å
6.	QMEAN value	QMEAN	0.75	−10.91	−0.53	−1.64

it quickly invades the host tissues. While some bacteria use mobility to move along the vascular wall, others float plankton in the flow of vascular fluid. These bacteria eventually multiply and form clusters that obstruct the vascular system.[11] In short, the bacterium can enter the plant's vascular system, grow inside the host system, and eventually wilt the plant permanently.

R. solanacearum spreads through various plant tissues by utilizing several virulence determinants.[12] The type III secretion system, also known as the T3SS, is the primary determinant of virulence in this pathogenic bacterium. This system shuttles effector proteins inside the host plant and modulates the cellular mechanism for the benefit of the microbe, thus proving to be crucial for the pathogenicity of the bacterium.[13] Exopolysaccharide (EPS) is a vital component of virulence.[14] In addition to clogging vascular tissue and harming the plant, EPS can attach to the bacterial cell wall and protect it from the plant's defense mechanism reaction. The physiological causes of wilting are complex. According to biochemical and genetic studies, the secreted enzymes polygalacturonase (PG) and endoglucanase (Egl), which break down plant cell walls, are also required for full virulence in addition to T3SS and EPS.[15]

In *R. solanacearum*, Allen et al.[15] discovered a regulatory locus called *pehSR* that regulates the virulence gene PG production. The NtrB/C subfamily of the two-component regulatory system (TRS) includes this locus, which consists of PehS and PehR.[15] Bacteria have evolved typical signal transduction systems like TRS to recognize and respond to ongoing changes in their environment.[16] The TRS typically consists of two distinct protein types: a membrane-associated sensor kinase and an effector cytosolic response regulator. These proteins regulate transcription, which, in turn, affects several crucial physiological processes. As a result, they are vital to the survival and pathogenicity of the bacterium, making them desirable targets for cutting-edge antibacterial medications.[17] Although PehR, an ATP-binding regulator, is essential for controlling PG production and motility in *R. solanacearum*, little is known about its precise structure and interaction pattern.

Since the molecular structure of PehR is unknown, the structural effects of PehR on ATP binding have also not been thoroughly investigated. In the current study, efforts have been made for the first time to generate the 3D structures of the PehR regulator and to identify the potential of its regulatory process to bind with ATP using cutting-edge *in silico* and *in vitro* methods. By identifying potential binding residues in the PehR regulator of *R. solancearum*, this study sheds light on the PehR-ATP complex, which might ultimately help with future research into the regulatory mechanisms of various ATP-binding regulators in phytopathogens.

RESULTS AND DISCUSSION

Insights of the Structural Model of PehR. Understanding the structure of proteins can help us better understand how they work, as they are the vital components of life. Thus, as shown in Table 1, we have used various modeling approaches to deduce the predicted PehR structural model. Results suggest that these predicted models met the majority of the validation criteria based on various servers after being validated using the various techniques listed in Table 1. Based on the findings in Table 1, we concluded that the PehR structural model predicted by AlphaFold has superior features. The NtrX crystal structure from *Brucella abortus* in complex with ATP (PDB ID: 5M7N)[18] was chosen as the template because it has the highest degree of similarity (37.8%) to the final PehR structural model, which has 570 amino acid residues.

The ProtParam tool (https://web.expasy.org/protparam/) was employed to calculate the various physicochemical characteristics of the PehR regulator. Although its molecular weight was estimated to be 61.59 kDa, the presumptive isoelectric point (pI),[19,20] which was 6.54 and nearly equal to 7, showed no noticeable difference in the proportion of negatively and positively charged residues. In terms of charge, negatively charged residues (Asp and Glu) made up 67 (11.75%), positively charged residues (Lys and Arg) made up 63 (11.05%), polar residues (Cys, Ser, Gln, Asn, Thr, Tyr, and His) made up 102 (17.90%), and hydrophobic residues (Ala, Gly, Ile, Leu, Met, Pro, Phe, Trp, and Val) made up 338 (59.30%) of the total amino acid residues present in PehR. A total of 8725 atoms were found in the PehR structure. Instability was found to exist as the solution instability index (Ii)[21] of value 49.05. PehR is a hydrophobic protein with a negative hydropathicity index (GRAVY)[22] with a large average (−0.083). The stability of the peptide was determined by its aliphatic index (Ai),[23] which measures stability over a range of temperatures, and it was found to be unstable at 97.79. In mammalian reticulocytes, yeast, and *E. coli*, PehR has a putative half-life[21] of close to 30, >20, and >10 h, respectively. The extinction coefficient (EC)[24] of PehR was calculated as 20,525 M^{-1} cm^{-1}.

https://doi.org/10.1021/acsomega.3c03175
ACS Omega 2023, 8, 34499−34515

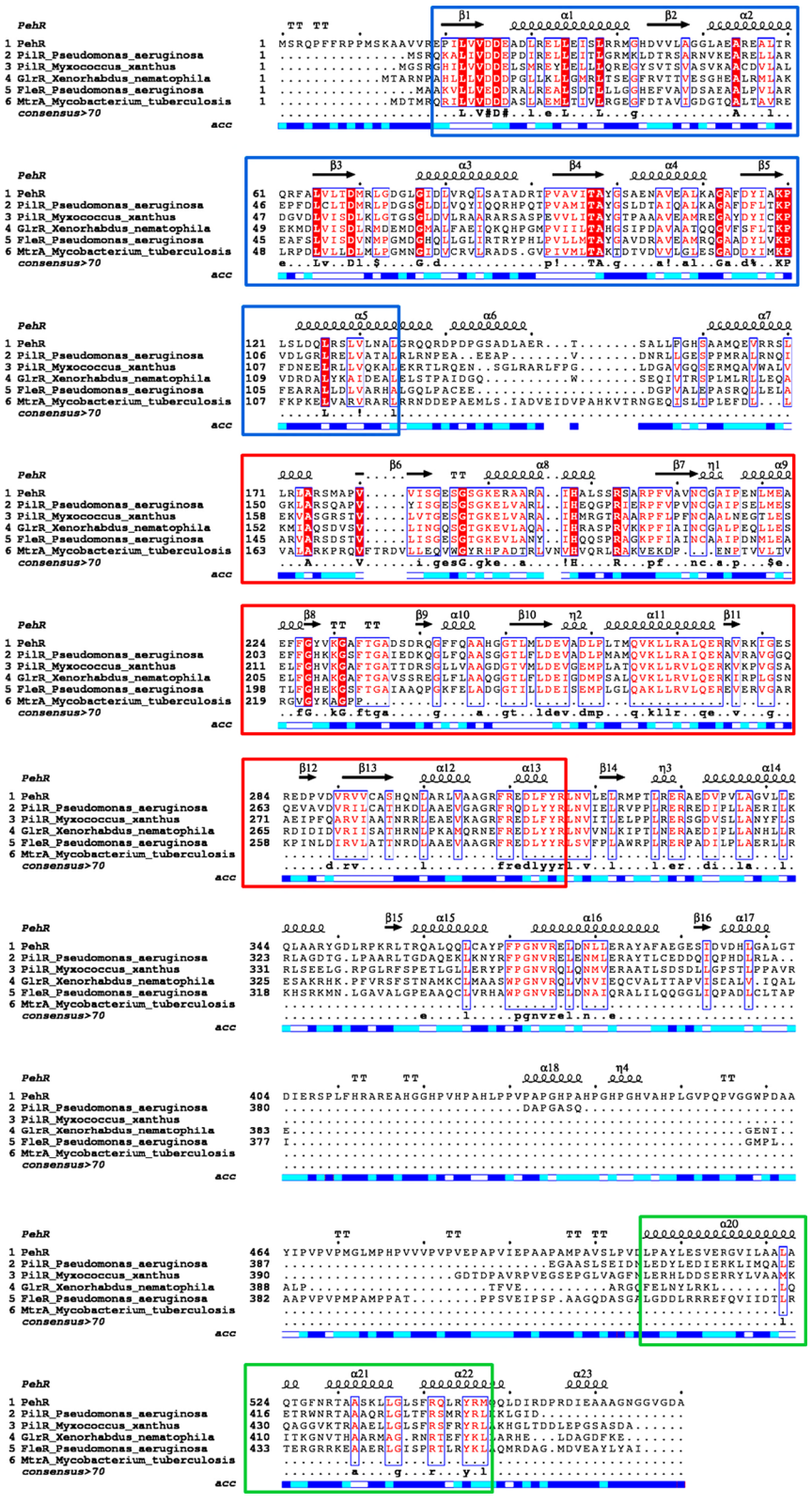

Figure 1. Multiple sequence alignment of six different transcriptional regulators. The PehR regulator was aligned with other transcriptional regulators from *P. aeruginosa*, *M. xanthus*, *X. nematophila*, and *M. tuberculosis* using MAFFT[25] and analyzed using ESPript 3.0.[26] The secondary structural elements of the PehR regulator are depicted at the top of the alignment. The dark red background columns show conserved identical residues, while the blue boxes show conserved residues of a similar nature. The AAA$^+$ ATPase domain is represented by a larger red box, the DNA-binding HTH domain by a larger green box, and the receiver domain by a larger blue box in the PehR regulator. Consensus sequences with >70% coverage are displayed at the bottom of the alignment.

https://doi.org/10.1021/acsomega.3c03175
ACS Omega 2023, 8, 34499−34515

As shown in Figure 1, to confirm the regulatory properties of PehR, we performed multiple sequence alignments with some other well-known bacterial transcriptional regulators, such as PilR, GlrR, FleR, and MtrA, from species like *Pseudomonas aeruginosa*, *Myxococcus xanthus*, *Xenorhabdus nematophila*, and *Mycobacterium tuberculosis*, respectively.[15]

Figure 1 shows the PehR secondary structural elements, which are consistent with the results of the Fourier transform infrared spectroscopy (FTIR) analysis discussed in the following sections. These elements include 44% helices, 16% beta-sheets, and 40% coiled structures. The PehR structure consists of 23 α-helices, 16 β-strands, and 20 coiled regions. The majority of transcriptional regulators are modular proteins with typically three domains.[27,28] First, the N-terminal response regulator receiver domain controls the activity of the regulatory proteins and contributes to signal perception. Second is the central AAA$^+$ ATPase domain that hydrolyzes ATP and is necessary and frequently sufficient to activate the sigma-54-dependent transcription.[27,29] Lastly, PehR has a helix-turn-helix (HTH) motif in its C-terminal DNA-binding domain, which aids in the identification of specific DNA-binding sites.[30−32] As shown in Figures 1 and 2, we discovered that the predicted PehR structure has all of these domains and belongs to the transcriptional regulatory protein family.

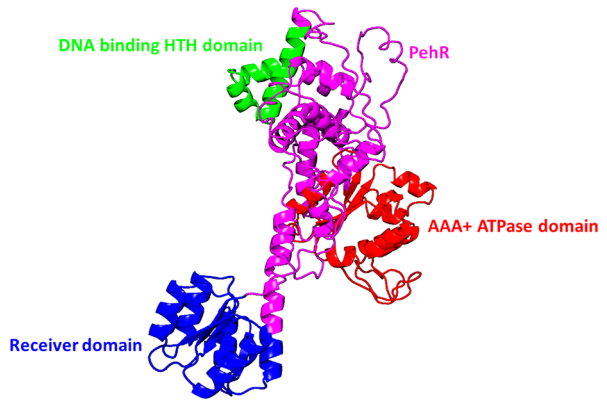

Figure 2. Structural organization of the PehR regulator from *R. solanacearum* F1C1. PehR tertiary structure model was generated in automated mode using the AlphaFold server (https://alphafold.ebi.ac.uk/), as described in the Materials and Methods section. The PehR domain characteristics are color-coded; the receiver domain (residues 19−130) is shown in blue, the AAA$^+$ ATPase domain (residues 176−320) is shown in red, and the DNA-binding HTH domain (residues 509−550) is shown in green.

As shown in Figures 1 and 2, the predicted PehR structure primarily consists of three domains: the receiver domain (residues 19−130), the effector domain, which includes an AAA$^+$ ATPase domain (residues 176−320), and the DNA-binding HTH domain (residues 509−550). Additionally, two low-complexity regions from residues 413 to 417 and residues 466 to 500 were noticed. From residues 167 to 397, the RNA polymerase sigma-54 interaction domain was also predicted. The PehR receptor domain, which is positioned above a DNA-binding effector domain in the TRS of *R. solanacearum*, is the domain that acquires signal from the sensor component. The regulatory domain undergoes conformational change as a result of being phosphorylated by the signal activity, activating an associated DNA-binding domain that regulates the response.[33] A histidine protein kinase sensor that phosphorylates the receiver domain of a response regulator makes up the two-component system in bacteria. As a result, the response regulator undergoes a conformational change that turns on the effector domain and sets off cellular reactions.[34]

The PehR receiver domain has a doubly wound five-stranded α/β fold with approximately 112 residues, as shown in Figure 2. A central five-stranded parallel β-sheet and five amphipathic α-helices on its either sides make up this fold. Leu, Val, Asp, Ala, Gly, Thr, Lys, and Pro are among the residues in the receiver domain that are highly conserved. RNA polymerase, which is connected to the sigma-54 factor and has an effector domain with about 230 residues necessary for the ATP-dependent association with sigma-54, recognizes the promoters of genes from which certain bacterial regulators turn them on.[35,36] This suggests that a conformational change needed for the association may require assistance from the 230-residue effector domain of the predicted PehR structure, which connects to the sigma-54 factor and has ATPase activity.[37] The PehR protein's central ATPase domain, also known as the AAA$^+$ module, has a length of about 145 amino acids and is structurally conserved. Typically, two structural subdomains make up the AAA$^+$ domain: a larger C-terminal all-α subdomain and a N-terminal P-loop ATPase $\alpha-\beta-\alpha$ subdomain (Figure 2). Ala, Val, Gly, His, and Arg are residues that have shown a high degree of conservation in these domains (Figure 1). The transcriptional regulator PehR, along with the other bacterial regulators shown in Figure 1—namely PilR, GlrR, FleR, and MtrA—encode HTH DNA-binding motifs in their C-terminal extremities. In this domain, the residues Leu, Ala, Gly, Arg, Gln, and Tyr were particularly conserved.

Molecular Docking and Ligand Interaction Analysis. By using the I-TASSER server's BioLiP, ATPbind, and COACH analyses,[38−40] we screened four ligands for the *R. solanacearum* F1C1 PehR homologue. These ligands were adenosine-5′-triphosphate (ATP), [[[(2R,3S,4R,5R)-5-(6-aminopurin-9-yl)-3,4-bis(oxidanyl)oxolan-2-yl]methoxy-oxidanyl-phosphoryl]oxy-oxidanyl-phosphoryl]oxy-tris(fluoranyl)-beryllium (08T), magnesium ion (Mg^{2+}), and 2,2-dimethylpropyl 2-[[3,5-bis(oxidanylidene)-2 ∼ {H}-1,2,4-triazin-6-yl]-sulfanyl]ethanoate (AZU). The adenine nucleotide ATP, which is found in all living cells, is composed of three phosphate groups esterified to the sugar moiety, while other nucleotide derivatives include 08T and AZU. These function as a cofactor, a fundamental metabolite, a micronutrient, and a nutraceutical.[41] The magnesium ion (Mg^{2+}) functions as a cofactor. Three different molecular docking experiments were run in AutoDock using the appropriate grid boxes to examine the probable mode of ligand binding in the final PehR structural model. The models with the highest docking scores demonstrating good ligand efficiency and hydrogen bonding were selected for further study from these various docking experiments (Figure 3).

The crystal ligand of NtrX (PDB ID: 5M7N)[18] was redocked against its binding site to test the molecular docking protocol used in AutoDock Vina. The same settings for the tested ligands, as listed in Materials and Methods, were used to prepare the cocrystallized ligand. The root-mean-square deviation (RMSD) was computed by superimposing the cocrystallized ligand, which served as the reference, with the docked ligand. The outcomes showed a value of 0.933 Å for NtrX, indicating a good degree of docking program accuracy (Figure S3).

https://doi.org/10.1021/acsomega.3c03175
ACS Omega 2023, 8, 34499−34515

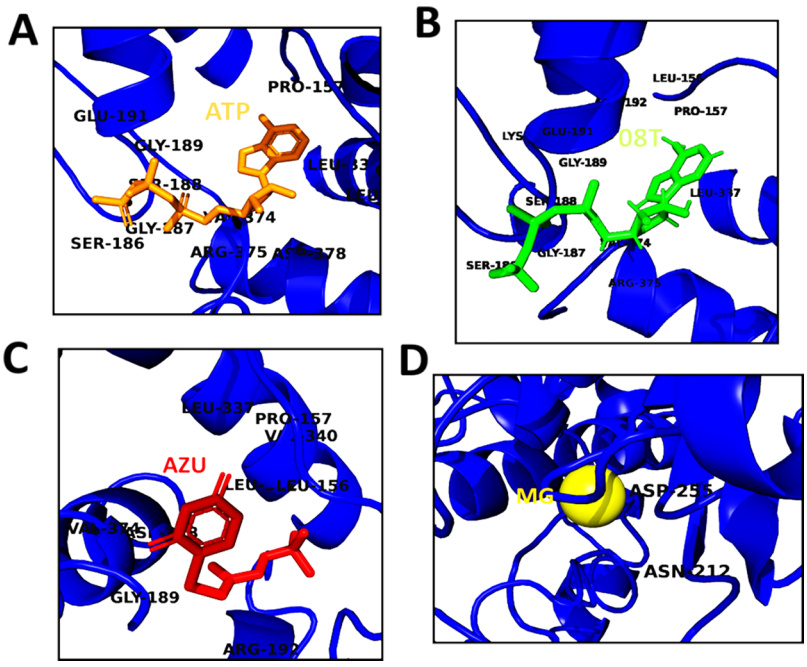

Figure 3. Illustrations of ligand binding for the PehR regulator from *R. solanacearum* F1C1. (A) PehR-ATP binding; PehR regulator is in blue cartoon shape, while ATP is in an orange stick shape; (B) PehR-08T binding; PehR regulator is in blue cartoon shape, while 08T is in green stick shape. (C) PehR-AZU binding; PehR regulator is in blue cartoon shape, while AZU is in red stick shape. (D) PehR-MG binding; PehR regulator is in blue cartoon shape, while MG is in a yellow round shape. In all illustrations, the interacting residues are highlighted.

To understand the role of different features involved in upholding the binding chemistry between PehR and its ligand complexes, the interatomic distances between the residues of these PehR complexes were closely examined (Figures 3 and 4 4). These calculations revealed that the PehR amino acids Pro^{157}, Ser^{186}, Gly^{187}, Gly^{188}, Gly^{189}, Glu^{191}, Arg^{330}, Leu^{337}, Gln^{341}, Val^{374}, Arg^{375}, and Asp^{378} were crucial for the tight attachment of ATP within the binding pocket via strong hydrogen bonds and nonpolar contacts (Figure 3A). The O_2 atom of ATP and Gly^{187} formed a potent H-bond at a mere 2.32 Å distance according to intermolecular analysis (Figure 4A). The intermolecular/interatomic distance plot (Figure 4A) revealed that the residues Lys^{190}, Glu^{191}, Arg^{192}, Arg^{375}, and Asp^{378} were directly in contact with ATP, whereas Pro^{157}, Ser^{186}, Gly^{189}, Leu^{337}, Val^{340}, Leu^{341}, Gln^{344}, Val^{374}, and Val^{446} showed intense nonpolar contacts with ATP. The precise connections of ATP with the PehR regulator are displayed in Figures 3A and 4A to better understand the PehR−ATP interaction mode.

As an ATP analogue for PehR, 08T binds in the amphipathic cavity created by the contributions of Leu^{156}, Pro^{157}, Gly^{158}, Ser^{186}, Gly^{187}, Ser^{188}, Gly^{189}, Lys^{190}, Glu^{191}, Arg^{192}, Asp^{255}, Glu^{256}, Leu^{337}, Val^{374}, and Arg^{375} residues (Figures 3B and 4B). Gly^{189} and Lys^{190} stabilize 08T through H-bonds, and Ser^{186}, Arg^{192}, Val^{374}, and Arg^{375} form direct interactions with 08T; Arg^{151}, Pro^{157}, Gly^{187}, Ser^{188}, Glu^{191}, Asp^{378}, and His^{445} form hydrophobic interactions with 08T (Figure 4B).

AZU was another important screened ligand for PehR. Additionally, it contained a strong *tert*-butyl analogue known as AZU but previously known as compound 12.[42] It functions as a LuxO inhibitor, the main NtrC-type response regulator in charge of regulating the entire *V. cholerae* QS cascade.[43] When AZU was docked with PehR to examine how the regulator's active site residues were recognized and localized, it was found that AZU was located in the same cavity as ATP on the surface of PehR (Figure 3C). AZU was found close to the side chains of the Gln^{344} amino acid of PehR. The hydrophobic interactions between AZU and Arg^{151}, Pro^{157}, Ser^{188}, Gly^{189}, Arg^{192}, and Val^{374} residues in the substrate-binding site of PehR stabilize its position (Figure 4C).

It has been established that the presence of divalent ions is required for both strong ATP-binding and ATPase activity.[44,45] The Mg^{2+} ion is important in bringing together the functional regions of the phosphate-binding domain.[46] As shown in Figure 3D, the Asn^{212} and Asp^{255} residues in PehR are the interaction sites for the Mg^{2+} ion; however, LigPlot$^+$ analysis failed to identify any interacting residues. Additionally, in ligand screening, the prediction was made using a C-score (confidence score), which has a range of [0−1], with a higher score indicating a more accurate prediction. The C-score represents the ligand binding with the ternary complexes. The C-scores for ATP, 08T, AZU, and Mg^{2+} were 0.81, 0.03, 0.02, and 0.01 respectively. In a further research, we used ATP in MD simulation analysis because the binding analysis and C-scores indicate that it was a more suitable ligand for PehR.

MD Simulation Analysis. MD simulation analysis was used to examine the inner movements, conformational switches, and binding longevity of ATP at the binding location of PehR. Figure 5 shows the trajectory analysis for the 200 ns MD simulation. The analysis of MD simulations was performed using the root-mean-square deviation (RMSD), root-mean-square fluctuation (RMSF), radius of gyration (Rg), hydrogen-bonding analysis, solvent accessible surface area (SASA), and principal component analysis (PCA).

Root-Mean-Square Deviation. The dynamic resilience and conformation of PehR and its complex with ATP and Mg^{2+} were assessed by calculating the RMSD for the C_α backbone during the 100 ns MD simulation using the equilibrated structure.[47] The RMSD measures the change in protein conformation between the two points on the trajectory.

https://doi.org/10.1021/acsomega.3c03175
ACS Omega 2023, 8, 34499−34515

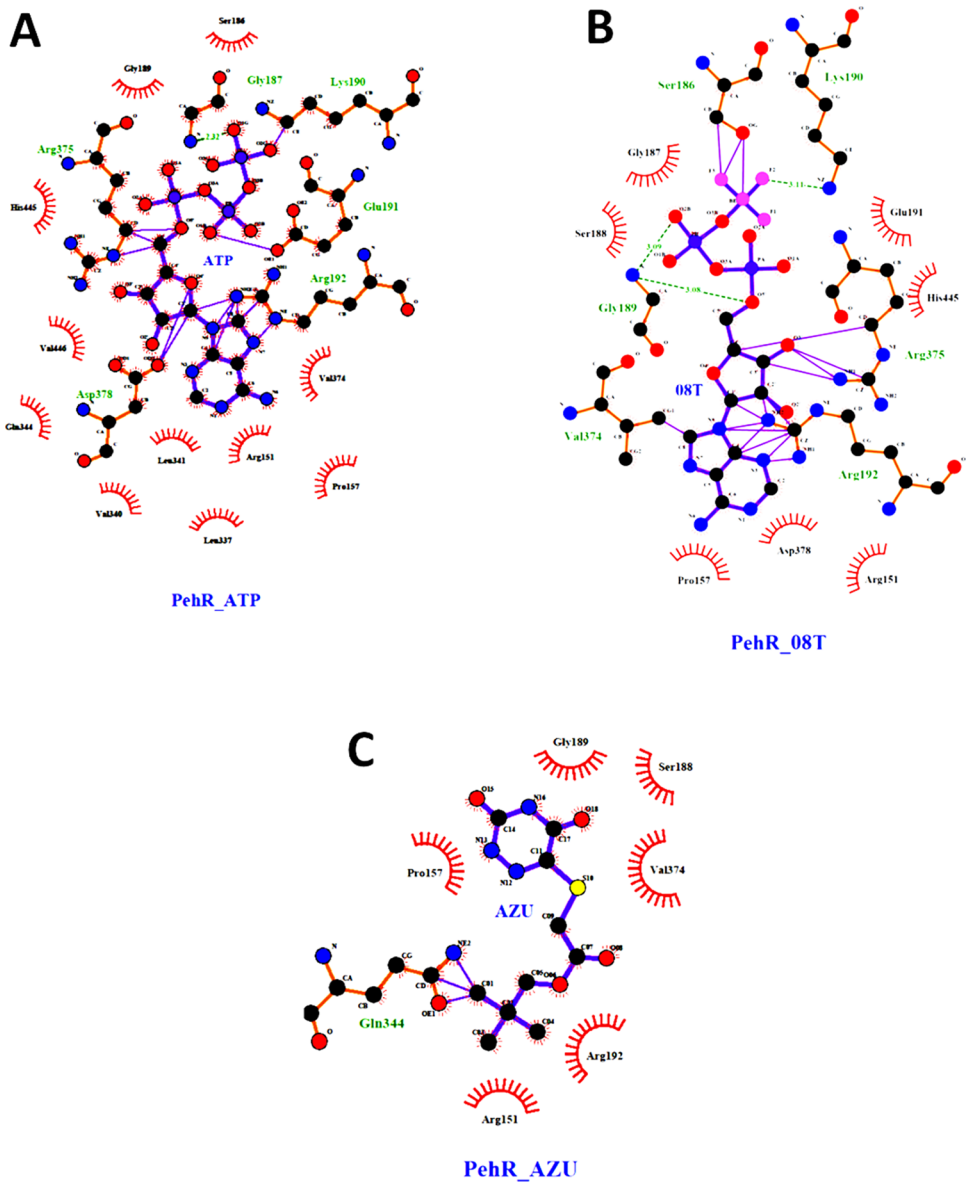

Figure 4. Outcomes of the LigPlot^{+} analysis. 2D representation of PehR−ligand interactions for (A) PehR-ATP, (B) PehR-08T, and (C) PehR-AZU. Hydrogen bonds are depicted as dark green dashed lines, with distances indicated in Å. The binding site residues of PehR are labeled in green, while additional PehR residues forming hydrophobic interactions with ATP are shown as red semicircles with radiating spokes.

Although the PehR-ATP and PehR-ATP-Mg^{2+} complexes (Figure 6) display a variety of RMSD patterns, the system stabilizes after 50 ns. The average RMSD measures for PehR-ATP, PehR, and PehR-ATP-Mg^{2+} complexes were 0.39 0.26, and 0.30 nm, respectively. For the 100 ns MD simulation, the PehR, ATP, and Mg^{2+} ions remained nearby the complex interface, which is consistent with a stable binding interaction. However, the loop-forming residues display slightly larger but random fluctuations throughout the 65−75 ns MD run, in contrast to the expectedly more constrained motion of helices and strands. The result indicates that both the PehR-ATP and PehR-ATP-Mg^{2+} complexes were largely stable during the simulation.

To investigate the potential role of Mg^{2+} ions in the binding of ATP to the binding site of PehR, we first performed MD simulations to simulate the structures bound to ATP to PehR in the presence and absence of Mg^{2+} ions, respectively (Figures S4 and 6). Then, using Autodock Vina in accordance with the Materials and Methods section, the affinity energies of the ATP ligand to the PehR protein were determined. The results suggested that the Mg^{2+} ions in the binding sites of PehR could increase the binding affinities of ATP to PehR because they showed that the affinity energies of the ATP ligand to PehR in the presence of Mg^{2+} ions are lower (−8.3 kcal/mol) than those in the absence of Mg^{2+} ions (−6.9 kcal/mol). We also calculated the RMSD during 100 ns of MD simulation to further characterize the bound conformations of ATP in the PehR binding site with and without Mg^{2+} ions. The average RMSD values for PehR with Mg^{2+} ions in the binding site were smaller (0.30 nm) than those without Mg^{2+} ions (0.39 nm), as shown in Figure 6, indicating that the conformations of the bound ATP ligand were more stable and less fluctuant during the simulations. This is in line with what has been seen in various X-ray crystal structures,[48−50] which show that Mg^{2+} ions are important for coordinating the phosphate tail of ATP in the binding sites.

https://doi.org/10.1021/acsomega.3c03175
ACS Omega 2023, 8, 34499−34515

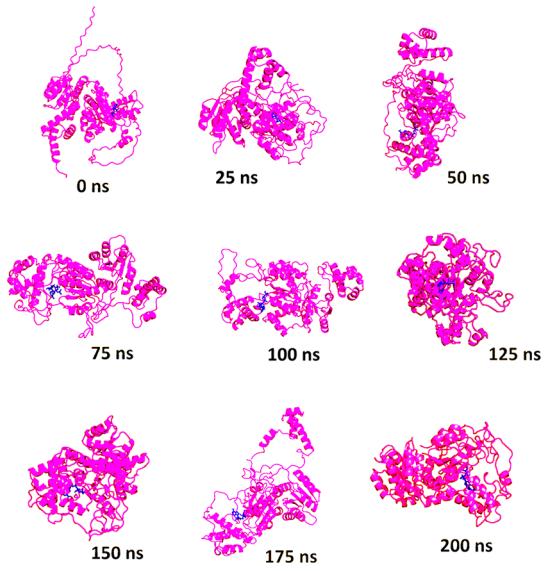

Figure 5. Snapshots taken from a simulation show the spontaneous self-assembly of PehR together with ATP during the 200 ns simulation period. In the illustration, ATP is represented by a blue stick and the PehR regulator by a pink cartoon character. To improve clarity, water molecules have been removed.

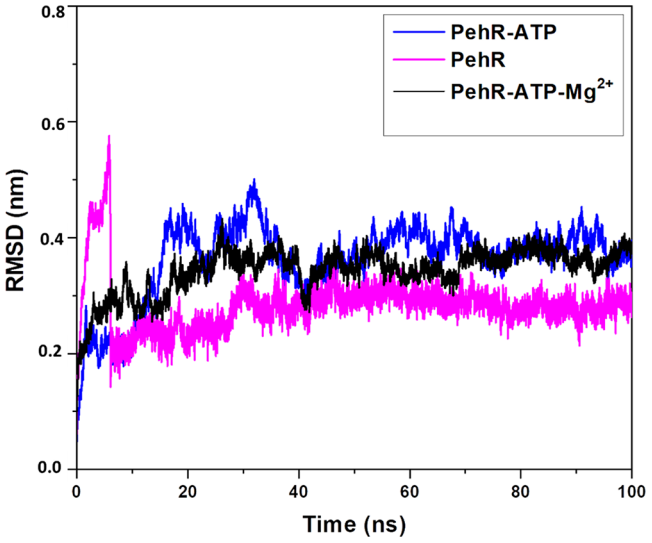

Figure 6. RMSD trends for the MD simulation trajectory of PehR, PehR-ATP, and PehR-ATP-Mg^{2+} complexes are shown in a 2D plot with a function of time.

Root-Mean-Square Fluctuation. The RMSF analysis can be used to distinguish between a protein's flexible and rigid regions (Figure 7). The RMSF of C atoms was calculated over the course of a 100 ns simulation. For structures like PehR, PehR-ATP, and PehR-ATP-Mg^{2+} complexes, the average RMSF was found to be 0.16 0.15, and 0.20 nm up to 420 residues, respectively. Higher fluctuations were visible in the residues (421 to 570) found in loops, turns, and terminal residues. The findings demonstrated that the average RMSF values of the PehR, PehR-ATP, and PehR-ATP-Mg^{2+} complexes were nearly similar and lower (up to 420 aa), which lessened the fluctuation in the protein-interacting site and stabilized the structure.

Radius of Gyration. The conformational geometry of the PehR, PehR-ATP, and PehR-ATP-Mg^{2+} complexes was

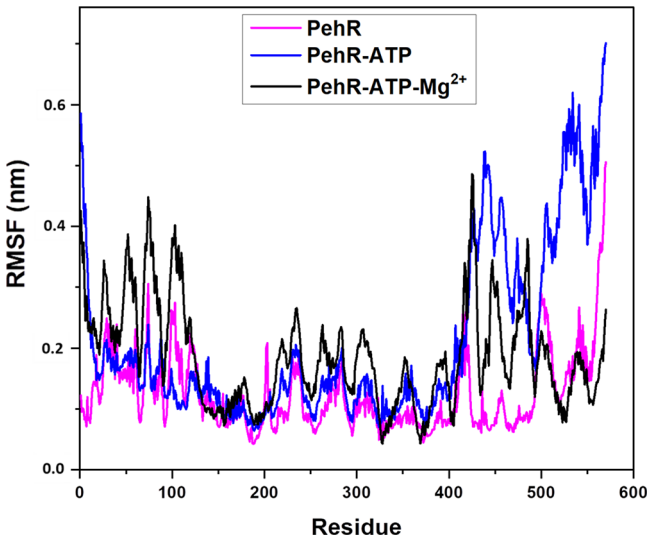

Figure 7. Two-dimensional plot produced over a 100 ns MD simulation period displays the RMSF trends for the MD simulation trajectory of PehR, PehR-ATP, and the PehR-ATP-Mg^{2+} complex.

calculated using the radius of gyration (Rg) (Figure 8). The Rg profile shows the degree of compactness and the pattern of

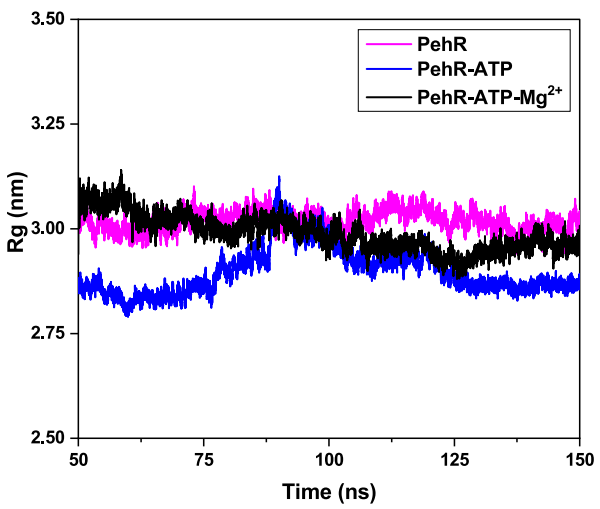

Figure 8. Two-dimensional plot displays the radius of gyration trend for a 100 ns MD simulation. In this plot, the pink, blue, and black lines denote the PehR regulator, PehR-ATP, and PehR-ATP-Mg^{2+} complexes, respectively.

protein folding. The average Rg values of PehR, PehR-ATP, and PehR-ATP-Mg^{2+} complexes were found to be 3.0, 2.8, and 3.0 nm, respectively. These numbers illustrate how similarly compact the structures were during the 100 ns MD run (Figure 8). Even though, as previously mentioned, significant fluctuations in the PehR protein were expected, the majority of the residues in the PehR-ATP and PehR-ATP-Mg^{2+} complexes maintained their stability throughout the MD run. Rg is, however, more likely to be moderately variable in the case of PehR-ATP, particularly in the loop regions. According to Rg profiles, the PehR-ATP-Mg^{2+} complex displayed its fundamental structure because there was some fluctuation, and it behaved compactly.

Hydrogen-Bonding Analysis. Hydrogen bonding is essential for the affinities and specificities of interactions in protein−

https://doi.org/10.1021/acsomega.3c03175
ACS Omega 2023, 8, 34499−34515

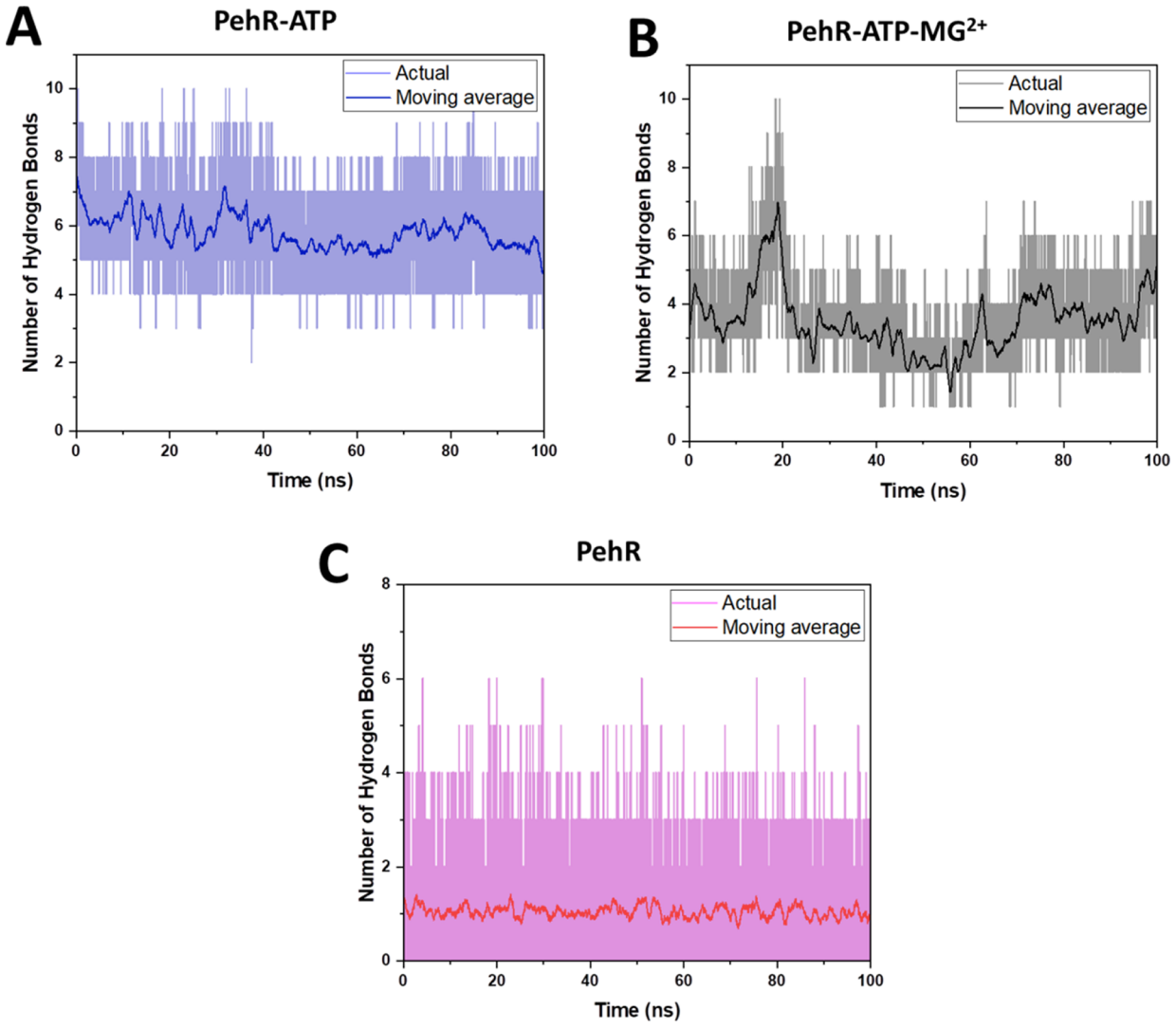

Figure 9. Two-dimensional plot of the H-bonds created overall for PehR, PehR-ATP, and PehR-ATP-Mg^{2+} complexes in the 100 ns MD simulation period. The PehR regulator and the PehR-ATP and PehR-ATP-Mg^{2+} complexes are indicated in this diagram by the pink, blue, and black lines, respectively. The solid lines are moving on average over 1000 ps.

ligand complexes.[51] We also investigated the hydrogen bonds in three structures, namely, PehR, PehR-ATP, and PehR-ATP-Mg^{2+} complexes. After a 100 ns MD simulation, Figure 9 depicts the integral number of hydrogen bonds in the structure of PehR and its complex with ATP and Mg^{2+} ions. The PehR-ATP and PehR-ATP-Mg^{2+} complexes showed more hydrogen bonds than did PehR by itself. There were 0−6, 2−10, and 1−10 hydrogen bonds in the PehR, PehR-ATP, and PehR-ATP-Mg^{2+} complexes, respectively. The findings showed that, throughout the 100 ns MD simulation process, ATP and Mg^{2+} ions had potent interactions with PehR, stabilizing the PehR structure, which may account for Mg^{2+} and ATP presence and its increased interacting surface area.

Solvent-Accessible Surface Area. To estimate the magnitude of the conformational changes that took place during the interaction, solvent-accessible surface area (SASA) of the PehR, PehR-ATP, and PehR-ATP-Mg^{2+} complexes was calculated. The percentage of the PehR regulator surface that was accessed by water solvent during MD simulation was calculated using the SASA parameter.[52] For the PehR, PehR-ATP, and PehR-ATP-Mg^{2+} complexes, the SASA value versus time has been plotted in Figure 10. The average SASA value

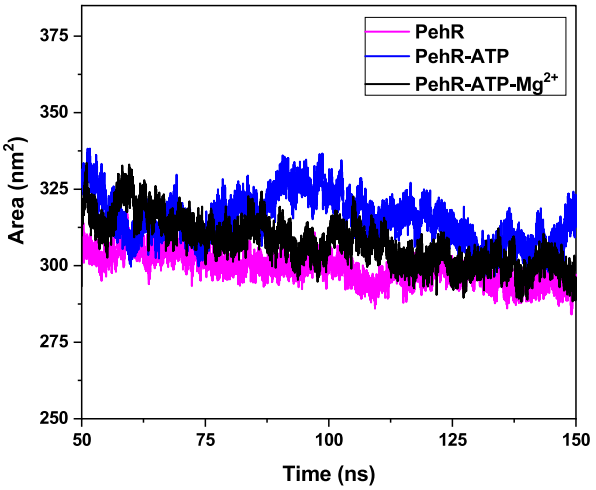

Figure 10. Time variation plot illustrating the solvent-accessible surface area (SASA) of the MD structures surrounding PehR (pink) and its complex with ATP (blue) and with Mg^{2+} (black).

https://doi.org/10.1021/acsomega.3c03175
ACS Omega 2023, 8, 34499−34515

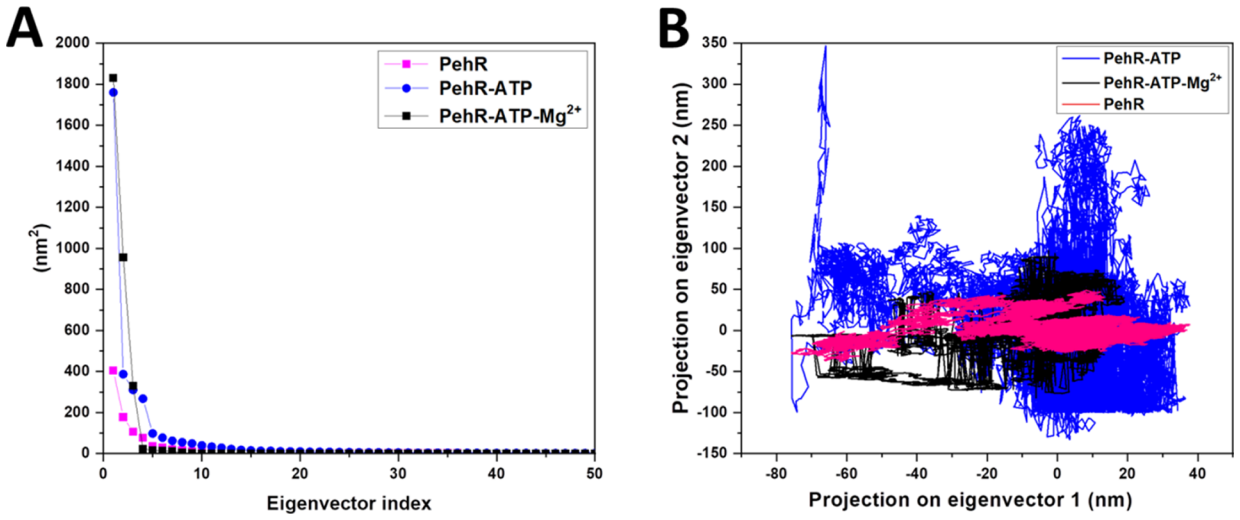

Figure 11. PCA of PehR, PehR-ATP, and PehR-ATP-Mg^{2+} complexes. (A) First 50 eigenvectors were plotted vs the eigenvalue of PehR, PehR-ATP, and PehR-ATP-Mg^{2+} complexes. (B) Collective motion of the PehR, PehR-ATP, and PehR-ATP-Mg^{2+} complexes is determined using projections of MD trajectories on two eigenvectors corresponding to the first two principal components.

for PehR was calculated to be 295.6 nm^2, and the average value for the PehR-ATP complex was 318.2 nm^2. While the average SASA value for PehR-ATP-Mg^{2+} was evaluated as 310.3 nm^2, the average SASA of the PehR-ATP and PehR-ATP-Mg^{2+} complexes was greater than that of PehR by itself in the MD simulation of a 100 ns trajectory period. The hydrophobicity increases with the increasing SASA value. Residues may be more capable to interact with ATP and Mg^{2+} ions because of their increased hydrophobicity. Consequently, we noted that the SASA values for the PehR-ATP and PehR-ATP-Mg^{2+} complexes during the 100 ns MD simulation were largely stable.

Principal Component Analysis. The essential dynamics (ED) technique was utilized to calculate the eigenvalues, eigenvectors, and their projection for the principal component analysis (PCA).[53,54] PCA assists in determining the general movement and substantial dynamics of the complex when PehR is bound to its substrate ATP and Mg^{2+} ions in an MD simulation (Figure 11). Using the analysis of PCA, the initial eigenvectors were determined, which are essential for the general movement of the PehR structural components during the MD simulation of the PehR, PehR-ATP, and PehR-ATP-Mg^{2+} complexes. As a result, in the analysis, it was decided to calculate the concerted motion using the first 50 eigenvectors. The eigenvalues and the corresponding eigenvectors are shown in Figure 11A for the PehR, PehR-ATP, and PehR-ATP-Mg^{2+} complexes. The first two eigenvector motion values of the PehR, PehR-ATP, and PehR-ATP-Mg^{2+} complexes, respectively, during the 100 ns MD simulation period are depicted in Figure 11A and accounted for almost more than 90% of the total motion. To further examine the dynamics of the PehR, PehR-ATP, and PehR-ATP-Mg^{2+} complexes via PCA, a 2D projection plot (Figure 11B) was made. We used PC1 and PC2 as the first two principal components of the analysis to focus on the important motion. In the 2D projection representation, the protein structures that are engaged in a smaller form of space are used to represent established assemblies, whereas the structures that are engaged in a larger form of space are used to represent unstable assemblies. Plotting the data revealed that the PehR-ATP-Mg^{2+} complex had a more compact cluster and consumed less phase space than the PehR-ATP complex (Figure 11B).

Cloning, Expression, and Purification of PehR Protein. Due to the highly guarded expression characteristics of *E. coli*, we used it as the host machinery for the cloning, expression, and purification analysis of the PehR regulator.[55−57] The homologous *pehR* gene (1713 bps), which encodes a 61.59 kDa protein, was cloned using a potent T7 promoter and an N-terminal 6xHis-tag-containing pET-28a(+) vector. A cloning method based on the polymerase chain reaction (PCR) was used to create the expression construct. A schematic illustration of the recombinant construct developed for this study is shown in Figure S1. The cloned construct was subsequently subjected to colony PCR using gene-specific primers and restriction enzyme digestion (by *Bam*HI and *Hin*dIII), and further, DNA sequencing using T7 forward and reverse primers was done for the confirmation of the in-frame cloning of the *pehR* gene and to check the accuracy of the sequence (Figure S2, and coding sequences are provided in Table S3).

E. coli cells transformed with the recombinant construct pMY (Table S1) underwent preliminary shake flask expression studies. Cells were induced with 0.1 mM isopropyl β-D-1-thiogalactopyranoside (IPTG) at a cell biomass (OD_{600}) of ∼0.5 to conduct expression studies in Luria−Bertani (LB) medium. The sodium dodecyl sulfate-polyacrylamide gel electrophoresis (SDS-PAGE) results at ∼61.0 kDa were consistent with the theoretically predicted molecular weight of the PehR protein, which contained only a 6xHis-tag (Figure 12). Regular measurements of cell growth were taken to look into the potential adverse effects of heterologous protein expression on the physiology of the cell. SDS-PAGE clearly showed that up to 6 h after induction, the accumulation of recombinant protein (∼61.0 kDa) increased continuously (Figure 12). Higher transcription rates cause the formation of insoluble aggregates, so the impact of the inducer concentration and cultivation temperature on protein solubility was also investigated.[58] For the production of recombinant PehR protein in *E. coli*, a temperature of 37 °C and 0.1 mM IPTG concentration were found to be ideal, and the expression profile is depicted in Figure 12. We used Ni-NTA affinity

https://doi.org/10.1021/acsomega.3c03175
ACS Omega 2023, 8, 34499−34515

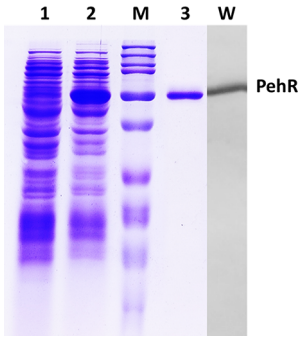

Figure 12. Overexpression and purification of the recombinant His-tagged PehR protein. Coomassie brilliant blue was used for protein detection. 12% SDS-PAGE gel demonstrating overexpression of recombinant His-tagged PehR protein in *E. coli* BL21(DE3) at 37 °C. Lane 1 is crude extract without IPTG induction, lane 2 is crude extract after 6 h of IPTG induction, lane M is molecular weight marker (Bio-Rad), lane 3 is purified His-tagged PehR protein fraction using Ni-NTA chromatography, and lane W is Western blot confirmation of His-tagged PehR protein with anti-His monoclonal antibody.

chromatography under native conditions to purify PehR, and as shown in Figure 12, a single band at roughly 61.0 kDa was found in the purified fraction in lane 3. This band's size was consistent with that of the recombinant PehR protein, which has a 6xHis-tag. Using primary anti-His and secondary HRP-conjugated antibodies, Western blot analysis confirmed our findings by revealing a single band at the 61.0 kDa position, further supporting the presence of the overexpressed PehR protein band (Figure 12).

PehR Exhibits Nucleotide (ATP)-Binding Activity. To confirm the binding of ATP with the PehR regulator, we examined the PehR-ATP complex using fluorescence spectroscopy and Fourier transform infrared spectroscopy.

R. solanacearum PehR Binds to a Fluorescent ATP Analogue. The fluorescent ATP analogue, 2′, 3′-O-trinitrophenol (TNP)-ATP, is a useful tool for investigating the nucleotide-binding sites of numerous bacterial proteins, including some ATPases.[59−62] The TNP-ATP was thoroughly characterized biochemically and biophysically, and it was found to be present in the nucleotide-binding site of the bacterial ATPases TraE, TraJ, and TraK.[59] In solution, TNP-ATP alone exhibits very little fluorescence. However, when it binds to proteins, there is a noticeable increase in fluorescence. In this study, fluorescence spectroscopy was employed to study the interaction of TNP-ATP with the PehR regulator. We used 2.5 μM concentration, as was determined to be optimal by Nandi et al.,[60] when titrating with a small heat shock protein HSP18. The maximum emission wavelength (from 560 to 540 nm) shifted to blue (Figure 13A), and the emission intensity was noticeably higher when TNP-ATP was bound to the PehR

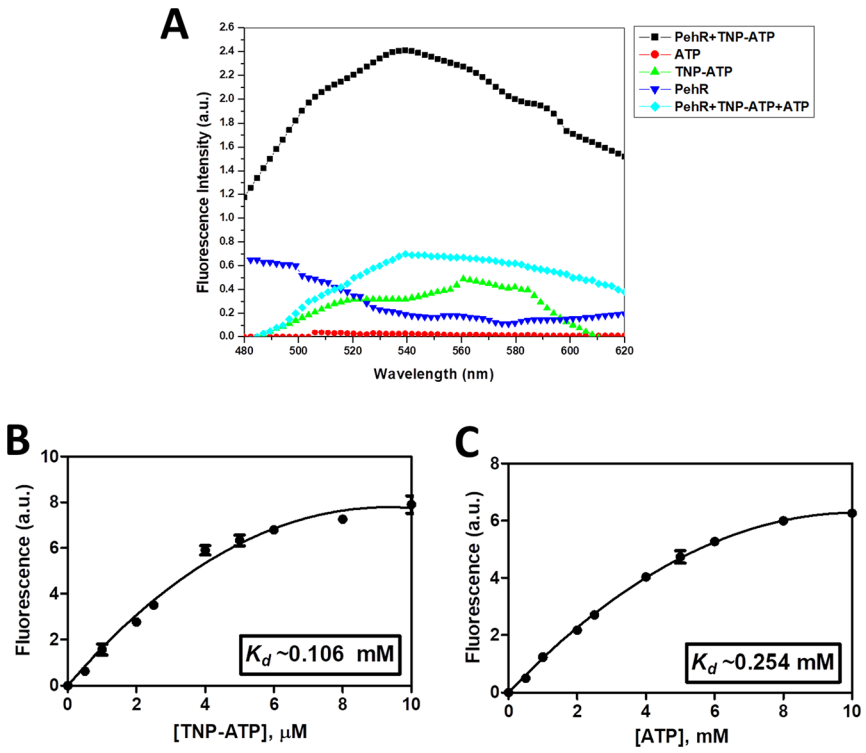

Figure 13. Nucleotide-binding assay of PehR. (A) Fluorescence emission spectra of the ATP, TNP-ATP, PehR, PehR+TNP-ATP, and PehR +TNP-ATP+ATP complexes. ATP (red circles), TNP-ATP (green triangles), PehR (dark blue triangles), PehR+TNP-ATP complex (black squares), and PehR+TNP-ATP+ATP complex (light blue square), show an emission wavelength range of 480−620 nm with an excitation wavelength of 410 nm. (B) Determination of the PehR+TNP-ATP dissociation constant (K_d). TNP-ATP is directly titrated into PehR-containing solutions, forming the PehR+TNP-ATP complex in a concentration-dependent manner. The K_d value of the PehR+TNP−ATP interaction was calculated to be 0.106 mM by fitting the fluorescent units against the TNP-ATP concentration to a Langmuir single-site binding equation. (C) For PehR binding, ATP competes with TNP-ATP. When ATP is titrated into a PehR+TNP-ATP complex solution, TNP-ATP is displaced, which reduces the fluorescence. The K_d value of the PehR+TNP−ATP+ATP interaction was calculated to be 0.254 mM by fitting a curve to the plot of the fraction of TNP-ATP-bound versus the ATP concentration. Data points represent the average of three determinations per concentration, and error bars represent the standard deviation. The data are representative of three independent experiments.

https://doi.org/10.1021/acsomega.3c03175
ACS Omega 2023, 8, 34499−34515

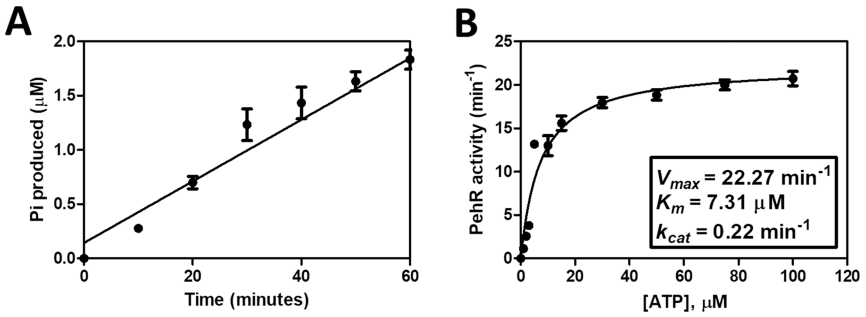

Figure 14. PehR ATPase activity assay. (A) ATP hydrolysis of PehR using an ATPase activity assay kit (MAK113, Sigma-Aldrich). At 1 mM ATP concentration, with 3 mM PehR, the rate of the reaction as calculated from the slope of the curve is 0.0284 mM Pi produced/min. (B) Michaelis−Menten curve was plotted with ATP concentrations in the range of 2−100 μM, and kinetic parameters are derived from the curve. Data points represent the average of three determinations per concentration, and error bars represent the standard deviation. Data are representative of three independent experiments.

protein. These findings suggested that, within the PehR protein, TNP-ATP had been moved from the polar to the nonpolar medium.

The two levels of the TNP−ATP interaction with proteins are an ambiguous association of the TNP moiety with nonpolar amino acids close to the ATP-binding pocket and a particular association with the ATP-binding region.[61] When the calibration curve for free TNP-ATP is linear (not shown), the fluorescent titration of PehR (2.5 μM) with increasing concentrations of TNP-ATP was carried out at concentrations between 1 and 10 μM. Data from the titration were recorded using the analytical program GraphPad Prism 7.0. With an R^2 value of 0.98 for curve fitting, we calculated the dissociation constant, K_d, for the PehR+TNP−ATP interaction to be 0.106 mM (Figure 13B). By adding too much ATP, TNP-ATP is gradually removed from the nonspecific binding sites, removing the nonspecific component (Figure 13C). By using the displacement assay to remove TNP-ATP from the PehR +TNP-ATP complex, we were able to determine the K_d value of ATP's affinity for PehR. The PehR+TNP-ATP complex was titrated with ATP. After a concentration-dependent decrease in fluorescence, free TNP-ATP levels were reached (Figure 13C), indicating the complete displacement of the fluorescent TNP-ATP. To determine the dissociation constant of unmodified ATP for PehR, the fraction of TNP-ATP bound was plotted against the concentration of ATP and fitted to an equation describing the competitive binding (see Materials and Methods for more information). Using curve fitting, we found the K_d value to be 0.254 mM with an R^2 value of 0.96 (Figure 13C). As shown by the light blue spectrum in Figure 13A, the PehR protein was combined with TNP-ATP before ATP was added to this complex. The intensity of TNP-ATP fluorescence was significantly reduced when 10 mM ATP was added to the PehR+TNP-ATP complex, suggesting that ATP can effectively remove TNP-ATP from the ATP-binding region in the PehR+TNP-ATP complex (Figure 13A). The fluorescence decreased as a result of the nonfluorescent nucleotide. In this type of experiment, ATP competes with TNP-ATP as a ligand.

FTIR Spectroscopy and ATPase Activity Analysis of PehR. Figure S5 depicts the distribution of chemical functional groups on the surfaces of ATP, PehR, and ATP-PehR using FTIR analysis. ATP, PehR, and ATP-PehR FTIR spectra were captured between 4000 and 400 cm^{-1}. Peaks in the ATP spectrum represent the stretching vibration of the surface −OH groups, the bending vibration of the assimilated solvent molecules, and the stretching vibration of the −OH groups (Figure S5), with peak positions at 3450, 1639, and 1111 cm^{-1}, respectively. The stretching vibrations of Mg(Al)−Si−O and Si−O−Si could be attributed to the peak at 1111 cm^{-1}.[63] The phosphate groups of ATP typically have an asymmetric stretching vibration between 1100 and 1300 cm^{-1}, and this vibration has a high absorption coefficient.[64]

The FTIR spectral data of protein molecules are typically interpreted by using the vibrations of their molecular components. These molecular components produce nine distinctive FTIR spectrum bands, which comprise amides A, B, and I−VII.[65] As shown in Figure S5, some of these distinct bands for PehR include amide-A (3450 cm^{-1}), amide-I (1639 cm^{-1}), amide-II (1550 cm^{-1}), amide-III (1294 cm^{-1}), and amide-IV (735 cm^{-1}). The amide-I (1700−1600 cm^{-1}) spectral region (expanded view in Figure S5), which is produced by the C═O stretching vibrations of the amino acid linkages along with the N−H bond bending and C−N bond stretches, is the most responsive to the secondary structural constituents of proteins.[66]

To further characterize the PehR-ATP binding, we then used a biochemical strategy (ATPase assay). Through structural analysis, we discovered that PehR contains the AAA^+ ATPase domain (residues 176−320), which is depicted in Figure 2, and that it may be a member of the ATPase family. The hydrolysis of ATP into ADP is catalyzed by ATPases, which are significant macromolecular biological enzymes, and a free phosphate ion, an ADP molecule, and energy are produced as the enzyme hydrolyzes ATP.[67,68] Therefore, ATPase activity was measured to assess the PehR regulator functionality. A colorimetric assay was used to calculate the amount of inorganic phosphate (Pi) liberated during ATP hydrolysis to directly study the ATPase activity, as illustrated in Figure 14A. A graph of PehR ATPase activity versus ATP concentration obtained from the assay is shown in Figure 14B, and the enzyme reaction was stopped by the addition of 200 μL of the reagent. Purified PehR hydrolyzes ATP in a time-dependent manner, with free phosphate rising linearly in 60 min, as shown in Figure 14A. At 1 mM ATP concentration, the rate of ATP hydrolysis, as calculated from the slope of the curve, was found to be 0.0284 mM/min. The ATPase activity of PehR was measured at different ATP concentrations and used to plot the Michaelis−Menten curve (Figure 14B). At that point, curve fitting allows the determination of k_{cat} and K_m values for PehR. The k_{cat} value (0.22 min^{-1}), K_m value (7.31

https://doi.org/10.1021/acsomega.3c03175
ACS Omega 2023, 8, 34499−34515

μM), and V_{max} value (22.27 min^{-1}) for PehR were calculated using GraphPad Prism software.

CONCLUSIONS

The molecular structure of the PehR regulator is not fully understood. As a result, the current work modeling the 3D structure of the PehR protein and using it to screen the potential binding partners could be applied to its regulatory process. A combined *in silico* and *in vitro* study can simply explain the structural changes required for the PehR regulator, which binds to nucleotides like ATP. Three domains are predicted to be present in the PehR regulator: a receiver domain at the N-terminus, an AAA^+ ATPase domain in the middle, and a DNA-binding HTH domain at the C-terminus. In this study, a computational approach, fluorescence spectroscopy, and FTIR analysis were employed to characterize how the PehR regulatory protein interacts with nucleotides (such as ATP and its derivatives, 08T, and AZU). The 3D structural model of the PehR regulator was docked with ATP, 08T, AZU, and the Mg^{2+} compound at their binding sites. The highest ranked docked PehR complex with ATP was further evaluated for stability through MD simulations. The individual chain fluctuations were higher in the PehR-ATP complex form compared to PehR alone, despite there being no discernible difference in the overall RMSD profiles of the docked complex and PehR alone. The structural analysis revealed similarities between PehR and other well-known bacterial transcriptional regulators, including PilR, GlrR, FleR, and MtrA from species including *P. aeruginosa*, *M. xanthus*, *X. nematophila*, and *M. tuberculosis*. The PehR regulator was synthesized recombinantly in *E. coli* cells for the *in vitro* method and purified to homogeneity using chromatographic methods. Furthermore, fluorescence spectroscopy and FTIR analysis were used to conduct experimental investigations into the interaction of the PehR-ATP complex. The outcome demonstrates that binding of ATP with PehR was primarily responsible for the complex formation, and the parameters highlight the fact that, as reported in MD simulation and binding studies, the PehR-ATP complex was stabilized by hydrogen bonds and hydrophobic interactions. The fluorescent ATP analogue TNP-ATP was employed in fluorescence spectroscopy to exploit the hints present in the binding environment of the complex to gain information about the PehR−ATP interaction. Our computational studies and spectroscopic experiments have confirmed the importance of the interactions between the amino acids Lys^{190}, Glu^{191}, Arg^{192}, Arg^{375}, and Asp^{378} in the formation of the PehR-ATP complex. Along with noncovalent interactions, hydrophobic interactions are essential for the binding of ATP in the cavity of PehR, thus creating a stable complex. The findings taken together strongly suggest that ATP is an effective ligand of the PehR regulator of the plant pathogenic bacterium *R. solanacearum*. The outcome of the current study, in our opinion, may pave the way for the structure-based design of novel PehR ligands that can effectively engage this highly desirable regulatory target.

MATERIALS AND METHODS

Chemicals, Strains, and Plasmids. Ingredients for the culture medium, antibiotics, and chemicals were purchased from HiMedia Laboratories. ThermoFisher Scientific provided the dNTPs, restriction endonucleases, T4 ligases, and DNA ladders (GeneRuler), while New England Biolabs (NEB) provided the Q5 high-fidelity DNA polymerase. The gel-extraction kits, plasmid DNA isolation kits, and genomic DNA isolation kits were procured from QIAGEN. Table S1 provides a detailed account of the plasmid and bacterial strains used, and Table S2 enlists the primers used in this study. *R. solanacearum* was grown at 28 °C and 150 rpm shaking conditions in a complete BG medium[69] which contained additional glucose (5 g/L). The BG medium consisted of bacterial peptone (10 g/L), casamino acids (1 g/L), and yeast extract (1 g/L). Agar (15 g/L) was added for plating purposes as and when required. *E. coli* DH5α (Invitrogen) was used as a cloning host, and the PehR protein expression was analyzed using *E. coli* BL21(DE3) (Novagen). Both of the *E. coli* strains were grown in LB medium and kept in an incubator with a temperature set at 37 °C and a shaking speed of 220 rpm. The medium was supplemented with the antibiotic kanamycin at the prescribed concentration of 50 g/mL. Integrated DNA Technologies (IDT) performed the primer synthesis.

Cloning of *pehR* gene. Using primers 1 and 2 (refer Table S2), *Bam*HI and *Hin*dIII restriction enzyme sites, and PCR, the *pehR* gene homologue from *R. solanacearum* F1C1 genome was amplified to a length of 1713 base pairs. The recombinant construct pMY was created by digesting both the amplified PCR product (1713 bp) and the plasmid vector pET-28a(+) with *Bam*HI and *Hin*dIII and then ligating the digested PCR product with the digested vector. The recommended procedure[57,70] was then used to transform the recombinant plasmid pMY into *E. coli* DH5α cells. In-frame fusion and precision of the cloned constructs were confirmed by double digestion, colony PCR, and DNA sequencing.

Protein Expression and Purification. The expression of the PehR protein was studied in *E. coli* cells. The recombinant strain MY2 was created by transforming *E. coli* BL21(DE3) cells with the construct pMY. The transformed cells (MY2) were added to LB broth that also contained 50 g/mL kanamycin, and the mixture was then incubated overnight at 37 °C. This was the primary culture. For the secondary culture, 1% v/v of the primary culture was added to 50 mL of LB broth. The culture was then incubated at 37 °C under 220 rpm shaking conditions. The culture was induced for 6 h at an OD_{600} value of roughly 0.5 by adding 0.1 mM of IPTG. 50 mL portion of the IPTG-induced bacterial culture was collected and then pelleted, followed by subsequent dissolution in 10 mL of lysis buffer (50 mM NaH_2PO_4, 300 mM NaCl, pH 8.0). To prepare the total cell lysate, cells were sonicated on ice for 20 cycles (10 s on/off) and then centrifuged at 12,000*g* for 30 min at 4 °C. The recombinant PehR protein was separated using Ni-NTA affinity chromatography. The Ni-NTA superflow column from QIAGEN was loaded with the soluble protein-containing supernatant. After the proteins had been passed, the column was washed with washing buffer (50 mM NaH_2PO_4, 300 mM NaCl and 20 mM imidazole, pH 8.0). Finally, the PehR protein was eluted using 10 mL of elution buffer (50 mM NaH_2PO_4, 300 mM NaCl, 250 mM imidazole, pH 8.0). Dialysis of the eluted protein was carried out overnight at 4 °C in dialysis buffer (50 mM NaH_2PO_4, 300 mM NaCl, 2 mM β-mercaptoethanol, 20% glycerol, pH 8.0). Using a Thermo Scientific NanoDrop 2000 system, the purity and protein concentration of the purified protein were assessed. Additionally, using the previously described protocol,[71] this protein was examined by running a 12% SDS-PAGE. Further confirmation was done via Western blotting using a mouse anti-His monoclonal primary antibody (Bio-Rad, USA).

https://doi.org/10.1021/acsomega.3c03175
ACS Omega 2023, 8, 34499−34515

ATP-Binding Assay. The ATP-binding assay was conducted in accordance with the methodology described in a previous study.[60] The substrate used was the fluorescent nucleotide analogue TNP-ATP from Invitrogen Life Sciences. In a nutshell, TNP-ATP (10 mg/mL) was incubated with protein containing 1 mg/mL (PehR) in 500 μL of reaction buffer (150 mM NaCl, 100 mM Tris-HCl (pH 7.4), 8 mM $MgAc_2$, 5% glycerol) for 5 min at room temperature. A biospectrometer (Eppendorf) was used to record the fluorescence spectra at room temperature, with excitation at 410 nm and emission ranging from 480 to 620 nm. The fluorescence maxima were established through graphical calculations. In a different experiment, the fluorescence titration of the recombinant PehR (2.5 μM in 150 mM NaCl, 100 mM Tris-HCl, 8 mM MgAc2, 5% glycerol, pH 7.4) with TNP-ATP was carried out in the range of 1−10 μM of TNP-ATP. Using the same spectrofluorometer as before, the fluorescence intensity of bound TNP-ATP was measured at 538 nm with an excitation wavelength of 410 nm. The fluorescent units against the TNP-ATP concentration were fitted to a Langmuir single-site binding equation using GraphPad Prism 7.0 analytical software (GraphPad Software, USA), and the dissociation constant (K_d) of the PehR+TNP−ATP interaction was calculated. Using a competitive binding assay,[72] we were able to calculate the K_d value for the competitor (ATP). The preincubated PehR+TNP-ATP complex received increasing amounts of ATP. Before fluorescence measurements, samples were gently shaken at room temperature for 5 min. GraphPad Prism 7.0 analytical software (GraphPad Software, USA) was used to fit the fluorescent units against the TNP-ATP concentration to a Langmuir single-site binding equation and determine the K_d value of the PehR+TNP−ATP+ATP interaction.

FTIR Spectroscopy Analysis. Using a PerkinElmer Spectrum-100 FTIR spectrometer, FTIR analysis was performed on the purified PehR protein, ATP, and their mixtures. The spectrum was recorded in the frequency range between 4000 and 400 cm^{-1}.[73] In a nutshell, FTIR measurements were carried out at pH 7.4 in 137 mM NaCl, 2.7 mM KCl, 10 mM Na_2HPO_4, 8 mM $MgAc_2$, and 1.8 mM KH_2PO_4. ATP and PehR were used at a 1:1 molar ratio. Using the average value of five different spectra acquired in this manner, Origin 6.0 software generated the final spectrum.

PehR ATPase Activity Assay. Using an ATPase activity assay kit (MAK113, Sigma-Aldrich), the ATPase activity of PehR was determined by monitoring the release of inorganic phosphate upon ATP hydrolysis. In a nutshell, purified PehR protein was prepared in assay buffer (40 mM Tris, 80 mM NaCl, 8 mM $MgAc_2$, 1 mM EDTA, pH 7.5) in a final volume of 2.0 mL at a final concentration of 0.5 mg/mL. As a negative control, BSA (final concentration, 0.5 mg/mL) was used. ATP (4 mM) was added to start the reaction, which was allowed to proceed for up to 60 min at room temperature, and samples were collected every 10 min. After incubating the last sample for 60 min, the reaction was stopped by adding 200 μL of the reagent included in the kit. A microplate reader (Thermo Fisher Scientific, Inc.) was used to measure the amount of released inorganic phosphate using a colorimetric reaction at 620 nm. The absorbance of a sample lacking PehR but otherwise treated identically was subtracted to account for the nonenzymatic hydrolysis of ATP. The rate of hydrolysis was determined for each concentration of ATP by linear regression analysis. K_m, k_{cat}, and V_{max} values were determined by fitting the Michaelis−Menten equation to a plot of PehR activity versus ATP concentration by using GraphPad Prism software.

Structural Modeling and Ligand Interaction. To create a higher-quality structural model for the PehR homologue of *R. solanacearum*, several structural models were created. For template-based structure prediction, the complete PehR sequence, which has 570 amino acids (Accession WP_011002714.1, Table S3), was taken from the protein sequence database (GenPept) of a program run by the National Center for Biotechnology Information (NCBI). Several modeling methods, such as the AlphaFold,[74,75] RaptorX,[76] I-TASSER,[77] and Hybrid methods,[78] were used to produce a high-quality model. Table S3 contains a list of template specifics, prediction results, and sequence identifiers. For comparative analysis, the top-scoring models (for PehR) with the highest C-score were selected as the final structure. These models were subjected to energy minimization to get rid of any steric clashes between side chains and to analyze the biophysical behavior in the dynamic system with GROMACS-2022.[79,80] The selected structural models were then subjected to quality evaluation using the programs MolProbity,[81] Verify3D,[82,83] Procheck,[84] ProSa II,[85] and Qmean.[86] The chosen metastable structure was subsequently employed for research on molecular docking and ligand binding. Each model was displayed using the molecular visualization program PyMOL ver. 2.5.4 (Schrödinger, 2022).[87] Numerous ligands for the *R. solanacearum* PehR homologue were screened using the BioLiP, ATPbind, and COACH analyses of the I-TASSER server.[38−40] The primary amino acid sequence of the PehR homologue was made available to the I-TASSER server (Table S3). The BioLip database was searched for ligand-binding template models using the TM-SITE and S-SITE methods.[39] To comprehend the binding pockets and the residues involved in the interactions between PehR and ATP, AutoDockVina[88] was used to molecularly dock the molecules. The LigPlot$^+$ analysis[89] was then used to supplement the findings. The energy-minimized PehR model was employed for the assessment of molecular docking calculations. An appropriate PDB format was created by downloading the "sdf" file (3D-conformer) for the ATP molecule from PubChem (https://pubchem.ncbi.nlm.nih.gov/). Hydrogen atoms were added, and charges (Kollman) were assigned using MGL Tools (https://ccsb.scripps.edu/mgltools/). PyMOL was used to clean all of the protein structures by removing heteroatoms and water molecules. The grid box's volume was set to 27,000 $Å^3$ to provide a sizable search area for docking. To target the ATP-binding cavity of PehR, a grid box for docking, with the center coordinates of $x = -1.88$, $y = 1.18$, $z = 6.40$, size 40 × 40 × 40 $Å^3$, and spacing 0.384 Å, was built. The ideal binding conformation was created by translation and rotation within the grid box that encloses the substrate-binding site at PehR. In the given grid space, default AutoDock Vina settings were used to dock PehR (grid dimensions as given; exhaustiveness= 8; energy range = 4). To evaluate the feasibility of the fit and make predictions about the potential side-chain interactions, each conformer was manually analyzed in PyMOL. When the grid search area exceeded 2700 $Å^2$, the exhaustiveness was then increased until convergence was attained (exhaustiveness = 100). Top-hit compounds were those with the lowest binding affinities according to the scoring function of AutoDock Vina, which categorized ligands according to their binding affinities, expressed in kcal/mol. The redocking method was used to validate the docking procedure.[90,91] The crystallographic

https://doi.org/10.1021/acsomega.3c03175
ACS Omega 2023, 8, 34499−34515

structure of NtrX (PDB ID: 5M7N, resolution: 2.90)[18] in complex with ATP was obtained using RCSB PDB (https://www.rcsb.org/). Using AutoDock Vina, the ATP from NtrX (chain A) was taken out and docked back into the active site. The cocrystallized complex was manually processed by opening it in a notepad, removing the ATP heteroatoms from the NtrX (chain A), pasting it into another notepad, and saving the result as a ligand in PDB file format. The procedure remained the same, including the grid parameters. This was done to make certain that the ligand binds precisely to the active site cleft and must exhibit less deviation from the actual cocrystallized complex. The RMSD was then computed by superimposing the redocked complex using PyMOL onto the reference cocrystallized complex. The best-docked model was selected for further investigation and used for MD simulation studies based on the lower energy and larger cluster size. At the end, LigPlot$^+$ v.1.4.5 software was used to substantiate the molecular interactions between protein−ligand complexes, including hydrogen bonds as well as the length of the bond.

Molecular Dynamics Simulation. MD simulation of PehR in complex with ATP was carried out to examine the binding mode of ATP with the AAA$^+$ domain of PehR, assess the stability of the PehR-ATP complex, and examine the conformational changes in PehR after ATP binding. Using the AutoDock results as a starting point, the best binding conformation of each complex was used for the GROMACS 2022.3 package MD simulations. The CHARMM 36 force field was used to create topologies for protein and protein−ligand complexes. Initially, the CGenFF server was used to generate the topology of ATP from the PehR-ATP complex, and partial charges were added for the preparation of the ATP ligand. After topology generation, the PehR-ATP complex was solvated in a cubic box with a volume of 986 nm^3, while a distance of 1.0 nm between each side was maintained using a simple point charge (spc216) water model. The final system contained 55354 water molecules and 5 Na^+ ions after the simulation system had been solvated and ionized with Na^+ ions at a concentration of 150 mM. In addition, these structures were relaxed using an energy-minimization method that involved the steepest descent algorithm running for 50,000 cycles until the maximum force was lower than 10 kJ/mol with the Verlet cutoff method. To avoid system distortion during the production simulation, a position-restrained equilibration run was performed following a 100 ps minimization run using the constant number, volume, and temperature (NVT) ensemble and the isothermal−isobaric (NPT) ensemble. The system was maintained at 300 K temperature and 1 atm pressure for 200 ns with a 2 fs time step using the simulation analysis, which was computed using the Parrinello−Rahman pressure coupling method[92] and the v-rescale temperature coupling method.[93] The particle mesh Ewald (PME) technique[94] was employed to estimate van der Waals as well as long-range electrostatic interactions, with a cutoff set at 1 nm for short-range van der Waals interactions. Using the LINCS algorithm[95] and a simulation time step of 0.002 ps, all bonds were constrained. After that, a 200 ns production simulation was finished.

Analysis of Molecular Dynamics Simulation Trajectory. The stability of the system in a water environment was assessed by using the MD trajectory files that were generated to display the deviation of each protein and complex. The GROMACS 2022.3 package functionalities were used to thoroughly examine the MD trajectory that resulted from the simulation. The PehR-ATP complex was examined using RMSD, RMSF, RG, SASA, and PCA. The structural analysis was carried out by analyzing the hydrogen bonds that formed between ATP and PehR during the 200 ns simulation using the H-bond utility in GROMACS 2022.3.

■ ASSOCIATED CONTENT

Supporting Information

The Supporting Information is available free of charge at https://pubs.acs.org/doi/10.1021/acsomega.3c03175.

List of strains and plasmids used in this study; list of primers used in this study; PehR nucleotide and amino acid sequences; schematic illustration of the *pehR* cloning strategy applied in this research; cloning of pET-28a(+)-*pehR* in *E. coli*, confirmed by colony PCR and restriction digestion analysis; RMSD values and superimposition; effect of $Mg2^+$ ions on the PehR-ATP complex structure; and comparison of PehR's FTIR spectrum for ATP binding (PDF)

■ AUTHOR INFORMATION

Corresponding Authors

Suvendra Kumar Ray − *Department of Molecular Biology and Biotechnology, Tezpur University, Napaam 784028 Assam, India*; Phone: +91-3712-275406; Email: suven@tezu.ernet.in

Aditya Kumar − *Department of Molecular Biology and Biotechnology, Tezpur University, Napaam 784028 Assam, India*; orcid.org/0000-0002-6474-8830; Phone: +91-3712-275403; Email: aditya@tezu.ernet.in

Authors

Mohit Yadav − *Department of Molecular Biology and Biotechnology, Tezpur University, Napaam 784028 Assam, India*; orcid.org/0000-0001-5171-5573

Sharmilee Sarkar − *Department of Molecular Biology and Biotechnology, Tezpur University, Napaam 784028 Assam, India*; orcid.org/0000-0001-5655-6874

Kaushika Olymon − *Department of Molecular Biology and Biotechnology, Tezpur University, Napaam 784028 Assam, India*; orcid.org/0000-0002-5031-6463

Complete contact information is available at: https://pubs.acs.org/10.1021/acsomega.3c03175

Author Contributions

#M.Y. and S.S. contributed equally to this work.

Funding

This work was supported by a core research grant from DST-SERB (**CRG/2020/002651**).

Notes

The authors declare no competing financial interest.

■ ACKNOWLEDGMENTS

The authors are grateful to the Science and Engineering Research Board (SERB), Department of Science and Technology (DST), Govt. of India, for the core research grant (**CRG/2020/002651**). M.Y. thanks SERB-DST for Research Associate (RA) Fellowship. S.S. is thankful to the Council of Scientific & Industrial Research (CSIR), Govt. of India, New Delhi, for the Senior Research Fellowship (SRF). K.O. is thankful to Tezpur University for the institutional fellowship.

REFERENCES

(1) Su, Y.; Xu, Y.; Liang, H.; Yuan, G.; Wu, X.; Zheng, D. Genome-Wide Identification of Ralstonia Solanacearum Genes Required for Survival in Tomato Plants. *mSystems* **2021**, *6* (5), No. e0083821.

(2) Wen, D.; Guo, Q.; Zhao, W.; Yang, Y.; Yang, C.; Yu, J.; Hu, Y. Effect and Mechanism of NaHS on Tobacco Bacterial Wilt Caused by Ralstonia Solanacearum. **123AD**. DOI: DOI: 10.1038/s41598-022-26697-8.

(3) Bai, W.; Kong, F.; Lin, Y.; Zhang, C. Extract of Syringa Oblata: A New Biocontrol Agent against Tobacco Bacterial Wilt Caused by Ralstonia Solanacearum. *Pestic. Biochem. Physiol.* **2016**, *134*, 79−83.

(4) Yuliar; Asi Nion, Y.; Toyota, K. Recent Trends in Control Methods for Bacterial Wilt Diseases Caused by Ralstonia Solanacearum. *Microbes Environ.* **2015**, *30* (1), 1.

(5) Mansfield, J.; Genin, S.; Magori, S.; Citovsky, V.; Sriariyanum, M.; Ronald, P.; Dow, M.; Verdier, V.; Beer, S. V.; Machado, M. A.; Toth, I.; Salmond, G.; Foster, G. D. Top 10 Plant Pathogenic Bacteria in Molecular Plant Pathology. *Mol. Plant Pathol.* **2012**, *13* (6), 614−629.

(6) Shi, H.; Liu, Y.; Ding, A.; Wang, W.; Sun, Y. Induced Defense Strategies of Plants against Ralstonia Solanacearum. *Front. Microbiol.* **2023**, *14*, No. 1059799.

(7) Elphinstone, J. G. The Current Bacterial Wilt Situation: A Global Overview. *Bact. wilt Dis. Ralstonia solanacearum species complex* **2005**, 9−28.

(8) Álvarez, B.; López, M. M.; Biosca, E. G. Influence of Native Microbiota on Survival of Ralstonia Solanacearum Phylotype II in River Water Microcosms. *Appl. Environ. Microbiol.* **2007**, *73* (22), 7210−7217.

(9) Hida, A.; Oku, S.; Kawasaki, T.; Nakashimada, Y.; Tajima, T.; Kato, J. Identification of the McpA and McpM Genes, Encoding Methyl-Accepting Proteins Involved in Amino Acid and l-Malate Chemotaxis, and Involvement of McpM-Mediated Chemotaxis in Plant Infection by Ralstonia Pseudosolanacearum (Formerly Ralstonia Solanacearum Phylotypes I and III). *Appl. Environ. Microbiol.* **2015**, *81* (21), 7420−7430.

(10) Tan, X.; Dai, X.; Chen, T.; Wu, Y.; Yang, D.; Zheng, Y.; Chen, H.; Wan, X.; Yang, Y. Complete Genome Sequence Analysis of Ralstonia Solanacearum Strain PeaFJ1 Provides Insights Into Its Strong Virulence in Peanut Plants. *Front. Microbiol.* **2022**, *13*, No. 830900.

(11) Caldwell, D.; Kim, B. S.; Iyer-Pascuzzi, A. S. Ralstonia Solanacearum Differentially Colonizes Roots of Resistant and Susceptible Tomato Plants. *Phytopathology* **2017**, *107* (5), 528−536.

(12) de Pedro-Jové, R.; Puigvert, M.; Sebastià, P.; Macho, A. P.; Monteiro, J. S.; Coll, N. S.; Setúbal, J. C.; Valls, M. Dynamic Expression of Ralstonia Solanacearum Virulence Factors and Metabolism-Controlling Genes during Plant Infection. *BMC Genomics* **2021**, *22*, 170.

(13) Peeters, N.; Carrère, S.; Anisimova, M.; Plener, L.; Cazalé, A. C.; Genin, S. Repertoire, Unified Nomenclature and Evolution of the Type III Effector Gene Set in the Ralstonia Solanacearum Species Complex. *BMC Genomics* **2013**, *14*, 859.

(14) Denny, T. P. Genetic Evidence That Extracellular Polysaccharide Is a Virulence Factor of Pseudomonas Solanacearum. *Mol. Plant-Microbe Interact.* **1991**, *4* (2), 198.

(15) Allen, C.; Gay, J.; Simon-Buela, L. A Regulatory Locus, PehSR, Controls Polygalacturonase Production and Other Virulence Functions in Ralstonia Solanacearum. *Mol. Plant-Microbe Interact.* **1997**, *10* (9), 1054−1064.

(16) Xie, Y.; Li, J.; Ding, Y.; Shao, X.; Sun, Y.; Xie, F.; Liu, S.; Tang, S.; Deng, X. An Atlas of Bacterial Two-Component Systems Reveals Function and Plasticity in Signal Transduction. *Cell Rep.* **2022**, *41* (3), No. 111502.

(17) Casado, J.; Lanas, Á.; González, A. Two-Component Regulatory Systems in Helicobacter Pylori and Campylobacter Jejuni: Attractive Targets for Novel Antibacterial Drugs. *Front. Cell. Infect. Microbiol.* **2022**, *12*, 1255.

(18) Fernández, I.; Cornaciu, I.; Carrica, M. del C.; Uchikawa, E.; Hoffmann, G.; Sieira, R.; Márquez, J. A.; Goldbaum, F. A. Three-Dimensional Structure of Full-Length NtrX, an Unusual Member of the NtrC Family of Response Regulators. *J. Mol. Biol.* **2017**, *429* (8), 1192−1212.

(19) Bjellqvist, B.; Hughes, G. J.; Pasquali, C.; Paquet, N.; Ravier, F.; Sanchez, J. -C; Frutiger, S.; Hochstrasser, D. The Focusing Positions of Polypeptides in Immobilized PH Gradients Can Be Predicted from Their Amino Acid Sequences. *Electrophoresis* **1993**, *14* (10), 1023−1031.

(20) Bjellqvist, B.; Basse, B.; Olsen, E.; Celis, J. E. Reference Points for Comparisons of Two-Dimensional Maps of Proteins from Different Human Cell Types Defined in a PH Scale Where Isoelectric Points Correlate with Polypeptide Compositions. *Electrophoresis* **1994**, *15* (3−4), 529−539.

(21) Gasteiger, E.; Hoogland, C.; Gattiker, A.; Duvaud, S.; Wilkins, M. R.; Appel, R. D.; Bairoch, A. The Proteomics Protocols Handbook. *Proteomics Protoc. Handb.* **2005**, 571−608.

(22) Kyte, J.; Doolittle, R. F. A Simple Method for Displaying the Hydropathic Character of a Protein. *J. Mol. Biol.* **1982**, *157* (1), 105−132.

(23) Atsushi, Ikai Thermostability and Aliphatic Index of Globular Proteins. *J. Biochem.* **1980**, *88* (6), 1895−1898.

(24) Gill, S. C.; von Hippel, P. H. Calculation of Protein Extinction Coefficients from Amino Acid Sequence Data. *Anal. Biochem.* **1989**, *182* (2), 319−326.

(25) Katoh, K.; Standley, D. M. MAFFT Multiple Sequence Alignment Software Version 7: Improvements in Performance and Usability. *Mol. Biol. Evol.* **2013**, *30* (4), 772−780.

(26) Robert, X.; Gouet, P. Deciphering Key Features in Protein Structures with the New ENDscript Server. *Nucleic Acids Res.* **2014**, *42* (W1), W320−W324.

(27) Schumacher, J.; Joly, N.; Rappas, M.; Zhang, X.; Buck, M. Structures and Organisation of AAA+ Enhancer Binding Proteins in Transcriptional Activation. *J. Struct. Biol.* **2006**, *156* (1), 190−199.

(28) Bush, M.; Dixon, R. The Role of Bacterial Enhancer Binding Proteins as Specialized Activators of Σ54-Dependent Transcription. *Microbiol. Mol. Biol. Rev.* **2012**, *76* (3), 497−529.

(29) Xu, H.; Gu, B.; Nixon, B. T.; Hoover, T. R. Purification and Characterization of the AAA+ Domain of Sinorhizobium Meliloti DctD, a Σ54-Dependent Transcriptional Activator. *J. Bacteriol.* **2004**, *186* (11), 3499.

(30) Pelton, J. G.; Kustu, S.; Wemmer, D. E. Solution Structure of the DNA-Binding Domain of NtrC with Three Alanine Substitutions. *J. Mol. Biol.* **1999**, *292* (5), 1095−1110.

(31) Sallai, L.; Tucker, P. A. Crystal Structure of the Central and C-Terminal Domain of the Sigma(54)-Activator ZraR. *J. Struct. Biol.* **2005**, *151* (2), 160−170.

(32) Yadav, M.; Rathore, J. S. In-Silico Analysis of Genomic Distribution and Functional Association of HipBA Toxin-Antitoxin (TA) Homologs in Entomopathogen Xenorhabdus Nematophila. *J. Asia-Pac. Entomol.* **2022**, *25* (3), No. 101949.

(33) West, A. H.; Stock, A. M. Histidine Kinases and Response Regulator Proteins in Two-Component Signaling Systems. *Trends Biochem. Sci.* **2001**, *26* (6), 369−376.

(34) Stock, A. M.; Robinson, V. L.; Goudreau, P. N. Two-Component Signal Transduction. *Annu. Rev. Biochem.* **2003**, *69*, 183−215.

(35) Morett, E.; Segovia, L. The Sigma 54 Bacterial Enhancer-Binding Protein Family: Mechanism of Action and Phylogenetic Relationship of Their Functional Domains. *J. Bacteriol.* **1993**, *175* (19), 6067−6074.

(36) Austin, S.; Kundrot, C.; Dixon, R. Influence of a Mutation in the Putative Nucleotide Binding Site of the Nitrogen Regulatory Protein NTRC on Its Positive Control Function. *Nucleic Acids Res.* **1991**, *19* (9), 2281−2287.

(37) Austin, S.; Dixon, R. The Prokaryotic Enhancer Binding Protein NTRC Has an ATPase Activity Which Is Phosphorylation and DNA Dependent. *EMBO J.* **1992**, *11* (6), 2219−2228.

https://doi.org/10.1021/acsomega.3c03175
ACS Omega 2023, 8, 34499−34515

(38) Yang, J.; Roy, A.; Zhang, Y. Protein−Ligand Binding Site Recognition Using Complementary Binding-Specific Substructure Comparison and Sequence Profile Alignment. *Bioinformatics* **2013**, *29* (20), 2588−2595, DOI: 10.1093/bioinformatics/btt447.
(39) Yang, J.; Roy, A.; Zhang, Y. BioLiP: A Semi-Manually Curated Database for Biologically Relevant Ligand−Protein Interactions. *Nucleic Acids Res.* **2013**, *41*, D1096.
(40) Hu, J.; Li, Y.; Zhang, Y.; Yu, D. J. ATPbind: Accurate Protein-ATP Binding Site Prediction by Combining Sequence-Profiling and Structure-Based Comparisons. *J. Chem. Inf. Model.* **2018**, *58* (2), 501−510.
(41) Kornberg, A. ATP and Inorganic Pyro- and Polyphosphate. *Protein Sci.* **1993**, *2* (1), 131−132.
(42) Ng, W. L.; Perez, L.; Cong, J.; Semmelhack, M. F.; Bassler, B. L. Broad Spectrum Pro-Quorum-Sensing Molecules as Inhibitors of Virulence in Vibrios. *PLoS Pathog.* **2012**, *8* (6), No. e1002767.
(43) Boyaci, H.; Shah, T.; Hurley, A.; Kokona, B.; Li, Z.; Ventocilla, C.; Jeffrey, P. D.; Semmelhack, M. F.; Fairman, R.; Bassler, B. L.; Hughson, F. M. Structure, Regulation, and Inhibition of the Quorum-Sensing Signal Integrator LuxO. *PLOS Biol.* **2016**, *14* (5), No. e1002464.
(44) Kanellopoulou, C.; George, A. B.; Masutani, E.; Cannons, J. L.; Ravell, J. C.; Yamamoto, T. N.; Smelkinson, M. G.; Jiang, P. Du; Matsuda-Lennikov, M.; Reilley, J.; Handon, R.; Lee, P. H.; Miller, J. R.; Restifo, N. P.; Zheng, L.; Schwartzberg, P. L.; Young, M.; Lenardo, M. J. Mg2+ Regulation of Kinase Signaling and Immune Function. *J. Exp. Med.* **2019**, *216* (8), 1828−1842.
(45) Souza, D. O. G.; De Meis, L. Calcium and Magnesium Regulation of Phosphorylation by ATP and ITP in Sarcoplasmic Reticulum Vesicles. *J. Biol. Chem.* **1976**, *251* (20), 6355−6359.
(46) Ihara, K.; Muraguchi, S.; Kato, M.; Shimizu, T.; Shirakawa, M.; Kuroda, S.; Kaibuchi, K.; Hakoshima, T. Crystal Structure of Human RhoA in a Dominantly Active Form Complexed with a GTP Analogue. *J. Biol. Chem.* **1998**, *273* (16), 9656−9666.
(47) Sargsyan, K.; Grauffel, C.; Lim, C. How Molecular Size Impacts RMSD Applications in Molecular Dynamics Simulations. *J. Chem. Theory Comput.* **2017**, *13* (4), 1518−1524.
(48) Frezza, E.; Martin, J.; Lavery, R. A Molecular Dynamics Study of Adenylyl Cyclase: The Impact of ATP and G-Protein Binding. *PLoS One* **2018**, *13* (4), No. e0196207.
(49) Ou, X.; Lao, Y.; Xu, J.; Wutthinitikornkit, Y.; Shi, R.; Chen, X.; Li, J. ATP Can Efficiently Stabilize Protein through a Unique Mechanism. *J. Am. Chem. Soc.* **2021**, *1* (10), 1766−1777.
(50) Yu, L.; Xu, L.; Xu, M.; Wan, B.; Yu, L.; Huang, Q. Role of Mg2+ Ions in Protein Kinase Phosphorylation: Insights from Molecular Dynamics Simulations of ATP-Kinase Complexes. *Mol. Simul.* **2011**, *37* (14), 1143−1150.
(51) Chen, D.; Oezguen, N.; Urvil, P.; Ferguson, C.; Dann, S. M.; Savidge, T. C. Regulation of Protein-Ligand Binding Affinity by Hydrogen Bond Pairing. *Sci. Adv.* **2016**, *2* (3), No. e1501240.
(52) Marsh, J. A.; Teichmann, S. A. Relative Solvent Accessible Surface Area Predicts Protein Conformational Changes upon Binding. *Structure* **2011**, *19* (6), 859.
(53) David, C. C.; Jacobs, D. J. Principal Component Analysis: A Method for Determining the Essential Dynamics of Proteins. *Methods Mol. Biol.* **2014**, *1084*, 193.
(54) Chaudhary, S.; Yadav, M.; Mathpal, S.; Chandra, S.; Rathore, J. S. Genomic Assortment and Interactive Insights of the Chromosomal Encoded Control of Cell Death (Ccd) Toxin-Antitoxin (TA) Module in Xenorhabdus Nematophila. *J. Biomol. Struct. Dyn.* **2022**, *41* (15), 7032−7044.
(55) Rosano, G. L.; Ceccarelli, E. A. Recombinant Protein Expression in Escherichia Coli: Advances and Challenges. *Front. Microbiol.* **2014**, *5*, 172.
(56) Yadav, M.; Rathore, J. S. Functional and Transcriptional Analysis of Chromosomal Encoded HipBAXn2 Type II Toxin-Antitoxin (TA) Module from Xenorhabdus Nematophila. *Microb. Pathog.* **2022**, *162*, No. 105309.
(57) Yadav, M.; Rathore, J. S. The HipBA Xn Operon from Xenorhabdus Nematophila Functions as a Bonafide Toxin-Antitoxin Module. *Appl. Microbiol. Biotechnol.* **2020**, *104*, 3081.
(58) de Marco, A. Strategies for Successful Recombinant Expression of Disulfide Bond-Dependent Proteins in Escherichia Coli. *Microb. Cell Fact.* **2009**, *8* (1), 26.
(59) Rangrez, A. Y.; Abajy, M. Y.; Keller, W.; Shouche, Y.; Grohmann, E. Biochemical Characterization of Three Putative ATPases from a New Type IV Secretion System of Aeromonas Veronii Plasmid PAC3249A. *BMC Biochem.* **2010**, *11* (1), 10.
(60) Nandi, S. K.; Chakraborty, A.; Panda, A. K.; Sinha Ray, S.; Kar, R. K.; Bhunia, A.; Biswas, A. Interaction of ATP with a Small Heat Shock Protein from Mycobacterium Leprae: Effect on Its Structure and Function. *PLoS Negl. Trop. Dis.* **2015**, *9* (3), No. e0003661.
(61) Hormaeche, I.; Alkorta, I.; Moro, F.; Valpuesta, J. M.; Goñi, F. M.; De la Cruz, F. D. Purification and Properties of TrwB, a Hexameric, ATP-Binding Integral Membrane Protein Essential for R388 Plasmid Conjugation. *J. Biol. Chem.* **2002**, *277* (48), 46456−46462.
(62) Guarnieri, M. T.; Blagg, B. S. J.; Zhao, R. A High-Throughput TNP-ATP Displacement Assay for Screening Inhibitors of ATP-Binding in Bacterial Histidine Kinases. *Assay Drug Dev. Technol.* **2011**, *9* (2), 174−183.
(63) Meng, F.; Song, M.; Chen, Y.; Wei, Y.; Song, B.; Cao, Q. Promoting Adsorption of Organic Pollutants via Tailoring Surface Physicochemical Properties of Biomass-Derived Carbon-Attapulgite. *Environ. Sci. Pollut. Res.* **2021**, *28* (9), 11106−11118.
(64) Syberg, F.; Suveyzdis, Y.; Kötting, C.; Gerwert, K.; Hofmann, E. Time-Resolved Fourier Transform Infrared Spectroscopy of the Nucleotide-Binding Domain from the ATP-Binding Cassette Transporter MsbA: ATP HYDROLYSIS IS THE RATE-LIMITING STEP IN THE CATALYTIC CYCLE*. *J. Biol. Chem.* **2012**, *287* (28), 23923.
(65) Krimm, S.; Bandekar, J. Vibrational Spectroscopy and Conformation of Peptides, Polypeptides, and Proteins. *Adv. Protein Chem.* **1986**, *38* (C), 181−364.
(66) Bandekar, J. Amide Modes and Protein Conformation. *Biochim. Biophys. Acta, Protein Struct. Mol. Enzymol.* **1992**, *1120* (2), 123−143.
(67) Wu, X.; Zhao, Y.; Zhang, H.; Yang, W.; Yang, J.; Sun, L.; Jiang, M.; Wang, Q.; Wang, Q.; Ye, X.; Zhang, X.; Wu, Y. Mechanism of Regulation of the Helicobacter Pylori Cagβ ATPase by CagZ. *Nat. Commun.* **2023**, *14* (1), 479.
(68) Bailly, A. P.; Perrin, A.; Serrano-Macia, M.; Maghames, C.; Leidecker, O.; Trauchessec, H.; Martinez-Chantar, M. L.; Gartner, A.; Xirodimas, D. P. The Balance between Mono- and NEDD8-Chains Controlled by NEDP1 upon DNA Damage Is a Regulatory Module of the HSP70 ATPase Activity. *Cell Rep.* **2019**, *29* (1), 212.e8−224.e8.
(69) Ray, S. K.; Kumar, R.; Peeters, N.; Boucher, C.; Genin, S. RpoN1, but Not RpoN2, Is Required for Twitching Motility, Natural Competence, Growth on Nitrate, and Virulence of Ralstonia Solanacearum. *Front. Microbiol.* **20156**, 229.
(70) Yadav, M.; Rathore, J. S. TAome Analysis of Type-II Toxin-Antitoxin System from Xenorhabdus Nematophila. *Comput. Biol. Chem.* **2018**, *76*, 293−301.
(71) Yadav, M.; Rathore, J. S. The HipBAXn Operon from Xenorhabdus Nematophila Functions as a Bonafide Toxin-Antitoxin Module. *Appl. Microbiol. Biotechnol.* **2020**, *104*, 3081.
(72) Longauer, B.; Bódis, E.; Lukács, A.; Barkó, S.; Nyitrai, M. Solubility and Thermal Stability of Thermotoga Maritima MreB. *Int. J. Mol. Sci.* **2022**, *23* (24), 16044.
(73) Singh, P. K.; Singh, J.; Medhi, T.; Kumar, A. Phytochemical Screening, Quantification, FT-IR Analysis, and in Silico Characterization of Potential Bio-Active Compounds Identified in HR-LC/MS Analysis of the Polyherbal Formulation from Northeast India. *ACS Omega* **2022**, *7* (37), 33067−33078.
(74) Varadi, M.; Anyango, S.; Deshpande, M.; Nair, S.; Natassia, C.; Yordanova, G.; Yuan, D.; Stroe, O.; Wood, G.; Laydon, A.; Zídek, A.; Green, T.; Tunyasuvunakool, K.; Petersen, S.; Jumper, J.; Clancy, E.; Green, R.; Vora, A.; Lutfi, M.; Figurnov, M.; Cowie, A.; Hobbs, N.;

Kohli, P.; Kleywegt, G.; Birney, E.; Hassabis, D.; Velankar, S. AlphaFold Protein Structure Database: Massively Expanding the Structural Coverage of Protein-Sequence Space with High-Accuracy Models. *Nucleic Acids Res.* **2022**, *50* (D1), D439−D444.
(75) Jumper, J.; Evans, R.; Pritzel, A.; Green, T.; Figurnov, M.; Ronneberger, O.; Tunyasuvunakool, K.; Bates, R.; Žídek, A.; Potapenko, A.; Bridgland, A.; Meyer, C.; Kohl, S. A. A.; Ballard, A. J.; Cowie, A.; Romera-Paredes, B.; Nikolov, S.; Jain, R.; Adler, J.; Back, T.; Petersen, S.; Reiman, D.; Clancy, E.; Zielinski, M.; Steinegger, M.; Pacholska, M.; Berghammer, T.; Bodenstein, S.; Silver, D.; Vinyals, O.; Senior, A. W.; Kavukcuoglu, K.; Kohli, P.; Hassabis, D. Highly Accurate Protein Structure Prediction with AlphaFold. *Nature* **2021**, *596* (7873), 583−589.
(76) Källberg, M.; Wang, H.; Wang, S.; Peng, J.; Wang, Z.; Lu, H.; Xu, J. Template-Based Protein Structure Modeling Using the RaptorX Web Server. *Nat. Protoc.* **2012**, *7* (8), 1511−1522.
(77) Yang, J.; Yan, R.; Roy, A.; Xu, D.; Poisson, J.; Zhang, Y. The I-TASSER Suite: Protein Structure and Function Prediction. *Nat. Methods* **2015**, *12* (1), 7−8.
(78) Dorn, M.; Breda, A.; Norberto De Souza, O. A Hybrid Method for the Protein Structure Prediction Problem. *Lect. Notes Comput. Sci.* **2008**, *5167 LNBI*, 47−56.
(79) Pronk, S.; Páll, S.; Schulz, R.; Larsson, P.; Bjelkmar, P.; Apostolov, R.; Shirts, M. R.; Smith, J. C.; Kasson, P. M.; Van Der Spoel, D.; Hess, B.; Lindahl, E. GROMACS 4.5: A High-Throughput and Highly Parallel Open Source Molecular Simulation Toolkit. *Bioinformatics* **2013**, *29* (7), 845−854.
(80) Abraham, M. J.; Murtola, T.; Schulz, R.; Páll, S.; Smith, J. C.; Hess, B.; Lindah, E. GROMACS: High Performance Molecular Simulations through Multi-Level Parallelism from Laptops to Supercomputers. *SoftwareX* **2015**, *1*−*2*, 19−25.
(81) Williams, C. J.; Headd, J. J.; Moriarty, N. W.; Prisant, M. G.; Videau, L. L.; Deis, L. N.; Verma, V.; Keedy, D. A.; Hintze, B. J.; Chen, V. B.; Jain, S.; Lewis, S. M.; Arendall, W. B.; Snoeyink, J.; Adams, P. D.; Lovell, S. C.; Richardson, J. S.; Richardson, D. C. MolProbity: More and Better Reference Data for Improved All-Atom Structure Validation. *Protein Sci.* **2018**, *27* (1), 293−315.
(82) Bowie, J. U.; Lüthy, R.; Eisenberg, D. A Method to Identify Protein Sequences That Fold into a Known Three-Dimensional Structure. *Science* **1991**, *253* (5016), 164−170.
(83) Lüthy, R.; Bowie, J. U.; Eisenberg, D. Assessment of Protein Models with Three-Dimensional Profiles. *Nature* **1992**, *356* (6364), 83−85.
(84) Laskowski, R. A.; MacArthur, M. W.; Moss, D. S.; Thornton, J. M.; IUCr. PROCHECK: A Program to Check the Stereochemical Quality of Protein Structures. *J. Appl. Crystallogr.* **1993**, *26* (2), 283−291.
(85) Sippl, M. J. Recognition of Errors in Three-Dimensional Structures of Proteins. *Proteins* **1993**, *17* (4), 355−362.
(86) Benkert, P.; Biasini, M.; Schwede, T. Toward the Estimation of the Absolute Quality of Individual Protein Structure Models. *Bioinformatics* **2011**, *27* (3), 343−350.
(87) Schrödinger, L. The PyMOL Molecular Graphics System, Version 1.8. https://www.pymol.org/citing (accessed June 2, 2017).
(88) Trott, O.; Olson, A. J. AutoDock Vina: Improving the Speed and Accuracy of Docking with a New Scoring Function, Efficient Optimization and Multithreading. *J. Comput. Chem.* **2010**, *31* (2), 455.
(89) Laskowski, R. A.; Swindells, M. B. LigPlot+: Multiple Ligand-Protein Interaction Diagrams for Drug Discovery. *J. Chem. Inf. Model.* **2011**, *51* (10), 2778−2786.
(90) Shivanika, C.; Deepak Kumar, S.; Ragunathan, V.; Tiwari, P.; Sumitha, A.; Brindha Devi, P. Molecular Docking, Validation, Dynamics Simulations, and Pharmacokinetic Prediction of Natural Compounds against the SARS-CoV-2 Main-Protease. *J. Biomol. Struct. Dyn.* **2022**, *40* (2), 585−611.
(91) Boulaamane, Y.; Kandpal, P.; Chandra, A.; Britel, M. R.; Maurady, A. Chemical Library Design, QSAR Modeling and Molecular Dynamics Simulations of Naturally Occurring Coumarins as Dual Inhibitors of MAO-B and AChE. *J. Biomol. Struct. Dyn.* **2023**, 1−18.
(92) Parrinello, M.; Rahman, A. Polymorphic Transitions in Single Crystals: A New Molecular Dynamics Method. *J. Appl. Phys.* **1998**, *52* (12), 7182.
(93) Bussi, G.; Donadio, D.; Parrinello, M. Canonical Sampling through Velocity Rescaling. *J. Chem. Phys.* **2007**, *126*, No. 014101.
(94) Essmann, U.; Perera, L.; Berkowitz, M. L.; Darden, T.; Lee, H.; Pedersen, L. G. A Smooth Particle Mesh Ewald Method. *J. Chem. Phys.* **1998**, *103* (19), 8577.
(95) Hess, B.; Bekker, H.; Berendsen, H. J. C.; Fraaije, J. G. E. M. LINCS: A Linear Constraint Solver for Molecular Simulations. *J. Comput. Chem.* **1997**, *18*, 14631472.

https://doi.org/10.1021/acsomega.3c03175
ACS Omega 2023, 8, 34499−34515